



**HAL**  
open science

# Experimental and numerical analysis of the Portevin-Le Chatelier effect in a nickel-base superalloy for turbine disks application

N. Guillermin, Jacques Besson, Alain Köster, L. Lacourt, Matthieu Mazière,  
H. Chalons, S. Forest

## ► To cite this version:

N. Guillermin, Jacques Besson, Alain Köster, L. Lacourt, Matthieu Mazière, et al.. Experimental and numerical analysis of the Portevin-Le Chatelier effect in a nickel-base superalloy for turbine disks application. *International Journal of Solids and Structures*, 2023, 264, pp.112076. 10.1016/j.ijsolstr.2022.112076 . hal-03905088

**HAL Id: hal-03905088**

**<https://hal.science/hal-03905088v1>**

Submitted on 17 Dec 2022

**HAL** is a multi-disciplinary open access archive for the deposit and dissemination of scientific research documents, whether they are published or not. The documents may come from teaching and research institutions in France or abroad, or from public or private research centers.

L'archive ouverte pluridisciplinaire **HAL**, est destinée au dépôt et à la diffusion de documents scientifiques de niveau recherche, publiés ou non, émanant des établissements d'enseignement et de recherche français ou étrangers, des laboratoires publics ou privés.

# Experimental and numerical analysis of the Portevin-Le Chatelier effect in a nickel-base superalloy for turbine disks application

N. Guillermin<sup>a,b</sup>, J. Besson<sup>a</sup>, A. Köster<sup>a</sup>, L. Lacourt<sup>a</sup>, M. Mazière<sup>a</sup>, H. Chalons<sup>b</sup> and S. Forest<sup>a,\*</sup>

<sup>a</sup>Mines Paris, PSL University, Centre des Matériaux, CNRS UMR 7633, BP 87, 91003 Evry, France

<sup>b</sup>SAFRAN Helicopter Engines, Avenue J.Slydowsky 64511 Bordes, France

---

## ARTICLE INFO

### Keywords:


Constitutive equations  
Viscoplasticity  
Nickel base superalloy  
Dynamic strain aging  
Negative strain rate sensitivity  
Portevin-Le Chatelier effect  
Bifurcation  
Strain localization  
DIC

## ABSTRACT

High-pressure turbine disks are subjected to extreme mechanical and thermal loadings throughout their lifetime. This is the reason why during the design of turboshaft engines, regulation rules impose on manufacturers to demonstrate the integrity of rotating parts, especially turbine disks, with over-speed experiments. To improve the prediction of rotation speed at burst, it is essential to study the viscoplastic behavior and the fracture of the material. The present work focuses on the approach used to calibrate accurately a viscoplastic behavior model at high temperature (500°C) of nickel-based superalloy Inconel718. The experimental testing campaign includes standard tensile tests on axisymmetric and flat specimens with and without notches. The behavior is described using the McCormick model for dynamic strain aging. This model accounts for the viscoplastic behavior including the range of negative strain rate sensitivity and the Portevin-Le Chatelier (PLC) effect. In addition to global measurements, digital image correlation at high temperature using a speckle directly engraved on the specimen is used to detect and measure the strain carried by the PLC bands. This information is used in the parameter calibration. The consideration of the machine stiffness is shown to be essential in the analysis for a correct description of serrations and of the critical strain for PLC effects. 3D simulations on full specimen geometries samples are performed to validate the finite element model. Finally, a full 3D representative disk geometry simulation is performed to detect instabilities and their propagation due to geometrical singularities.

---

\*Corresponding author

 [samuel.forest@minesparis.psl.eu](mailto:samuel.forest@minesparis.psl.eu) (S. Forest)

ORCID(s):

## 1. Introduction

High pressure turbine disks are subjected to extreme mechanical and thermal loadings. In order to improve the prediction of rotation speed at burst, it is essential to use an accurate behavior of the material (Mazière et al., 2009). During the design of turbine disks, two speed ranges need to be covered. On the one hand, regulation rules consist in demonstrating the resistance of the disk to overspeed conditions at a slow strain rate. On the other hand, accidental overspeed events can take place at higher strain rates.

Moreover, in most industrial materials loaded in a certain range of temperatures and strain rates, the Portevin-Le Chatelier (PLC) effect occurs causing an irregular plastic flow usually observed as stress serrations and acoustic emissions during elongation tests on coupons. The dynamic interaction between mobile dislocations and diffusing solute atoms is the reason explaining the serrations in the stress-strain curve due to a negative strain rate sensitivity of the flow stress according to Cottrell (1953b) and MacCormick (1988). The motion of mobile dislocations is an intermittent process. Solute atoms diffuse towards mobile and forest dislocations and temporarily pin them. The process is repeated dynamically during the plastic flow: Pinning and unpinning of mobile dislocations (Van den Beukel, 1980). A critical strain value has to be reached to activate serrated yielding and heterogenous plastic strain localization bands appear and propagate (Mazière et al., 2010). Dynamic strain aging (DSA) can be associated with a negative strain rate sensitivity in given range of strain rates and temperature. It can also affect the hardening rate of the material (Ren et al., 2017).

DSA has been already observed in many experimental studies on (i) Aluminum alloys like Al-Mg (Clausen et al., 2004; Amokhtar et al., 2006; Halim et al., 2007; Reyne et al., 2019) and Al-Cu (Ranc and Wagner, 2005; Böhlke et al., 2009) at room temperature, (ii) Ferritic C-Mn steels (Wang et al., 2012; Ranc et al., 2016; Ren et al., 2020; Lee et al., 2021) at around 300°C-400°C, (iii) Titanium alloys at around 400°C (Prasad and Varma, 2008; Marchenko et al., 2016), (iv) Cobalt-based superalloys at 600°C (Cui et al., 2011; Chaboche et al., 2013; Mazière and Andrebo, 2015). DSA effects are also mentioned in (v) high-strength Nickel-based superalloys tested at around 500°C as reported in (Fournier et al., 2001; Dudova et al., 2008; Cai et al., 2017) and more recently in (Song et al., 2021a; Zhang et al., 2021). The PLC phenomenon appears in a wide range of materials. This phenomenon remains however complex to identify and few works present an accurately calibrated numerical model on tests on various specimens.

For nickel-base materials, the identification of solute species involved in the occurrence of the PLC is established by calculating the apparent activation energies for the diffusion of various solute species in the alloy. An abundant literature based on nickel-based alloys exists with a description of various methods to determine the activation energies. At low temperature the PLC effect is attributed to the interaction between carbon atmosphere and mobile dislocations during plastic deformation (Chen and Chaturvedi, 1997; Hale et al., 2001). The occurrence of jerky flow has been ascribed to the effect of Cr (Hale et al., 2001), Nb (Hayes, 1983; Nalawade et al., 2008) and Mo (Max et al., 2014, 2018).

As imaging techniques and image resolution are constantly progressing, the observation of PLC effect is now possible with digital image correlation (DIC) and digital image thermography (DIT). In the works mentioned above, the DIC method is widely used to observe the PLC bands. Although this non-contact field measurement method allows to get more details about PLC –location, thickness, strain rate of the bands– than the macroscopic serrated curves, the latter is mostly used in the identification of a numerical model. Other experimental techniques, detailed in (Yilmaz, 2011), are more rarely encountered in the literature to describe instabilities such as the capture of acoustic emission waves to get a spatio-temporal evolution of events (Máthis et al., 2006; Louche et al., 2008) or the variation of the magnetic field (Dhar et al., 2002).

Industrial parts or structures in turboshaft engines have complex geometrical features, such as holes, fillets, and chamfers, inducing stress concentrations. In the presence of a notch, the highly inhomogeneous strain gradient makes these zones more sensitive to the PLC effect (Benallal et al., 2008). In uni-axial tensile tests, localization bands are usually found to nucleate in the curved region of the specimen's ends due to strain gradients. Until today, even though certification tests on real disk geometry are mandatory, there are no experimental techniques that allow seeing the appearance and the propagation of PLC bands during such tests on components. The experimental challenges can easily be understood considering that disks are rotating at more than several thousand rounds per minute and their dimensions are larger than standard laboratory specimens.

The current work aims to identify an elastoviscoplastic constitutive model that can reproduce the DSA (low or negative strain rate sensitivity) and PLC effects (propagation of strain rate localization bands) in the nickel-based superalloy IN718 used in helicopter turbine disks. The proposed model and associated finite element simulations must reproduce the macroscopic curves and DIC measurements for a large variety of tests ranging from simple tension to

notched specimens. The tests are carried out with displacement control at high temperature (500°C), considered as the critical in service temperature. Significant improvement of the quality of model prediction has been obtained by introducing the testing machine stiffness in the modeling, an essential feature which is very often not taken into account in the literature. Moreover, the finite element model is used to predict the results of a load-controlled test representative of real-life loadings in the turboshaft disk. The model and finite element simulations are formulated within the finite strain framework because large deformations are essential to predict the burst of turbine disks. Another original feature of the work is the use of a new speckle pattern technique that has been developed for DIC in order to better resist higher temperatures and higher strain levels compared to the usual painted speckles. Finally, 3D finite element simulations including are carried out on a realistic disk geometry to explore the PLC effects in a real component. Only few works in the literature provide simulations of the PLC effect in an industrial structure, see (Mazière et al., 2010b; Song et al., 2021b). In this sense this work presents a significant step forward for the introduction of dynamic strain aging in the design of turbine disks.

The paper is structured as follows. Section 2 presents the material while Section 3 details a new speckle engraved method, specimen geometries and testing conditions. Section 4 proposes a constitutive model applied in finite element simulations. Section 5 explains the identification strategy of the viscoplastic constitutive model. Then, section 6 exposes several validations of the model for other specimen geometries using displacement-controlled testing as well as load-controlled testing. Finally, section 7 discusses the validity range of the proposed model, the influence of a well-calibrated stiffness machine on simulations and finally a full structure application of the model on a realistic disk.

The mathematical notations used throughout the paper are the following: second order tensors are denoted by  $\underline{\underline{a}}$  (an example is the Cauchy stress tensor  $\underline{\underline{\sigma}}$ ) and fourth order tensors are written  $\underline{\underline{\underline{A}}}$  (an example is the elasticity tensor  $\underline{\underline{\underline{E}}}$ ).

## 2. Material

The investigated material is Inconel718 and has been developed since 1965 following the work of Eiselstein (1965). The addition of a new element, Niobium, led to the creation of this nickel-based superalloy with exceptional properties. The composition of Inconel718 is detailed in Table 1. This material is used for turbine disks in jet and helicopter engines (Ponnelle et al., 2002).

**Table 1**

Chemical composition of Inconel718 nickel-based superalloy Devarapalli et al. (2016).

| Wt [%] | Ni   | Fe   | Cr   | Nb  | Mo  | Ti   | Al  | C     |
|--------|------|------|------|-----|-----|------|-----|-------|
| Max    | Base | 21.0 | 21.0 | 5.5 | 3.3 | 1.15 | 0.7 | 0.040 |
| Min    | Base | 15.0 | 17.0 | 5.0 | 2.8 | 0.75 | 0.3 | 0.015 |

The final microstructure is made of several crystallographic phases presented by Sims et al. (1947). The  $\gamma$  phase is the most present phase in this alloy and is mainly composed of nickel with a face-centered cubic structure leading to a first hardening of the alloy by solid solution (Jena and Chaturvedi, 1984). The  $\gamma'$  –Ni<sub>3</sub>(Ti,Al)–, and  $\gamma''$  –Ni<sub>3</sub>Nb–, are the most important phases having exceptional mechanical characteristics. These hardening phases are formed at high temperatures during post-solidification cooling. The appearance of these phases in rough castings is localized in the interdendritic spaces (Gao and Wei, 1995; Miller et al., 2002). These precipitates are generally spherical for the  $\gamma'$  phase and disc-shaped for the  $\gamma''$  phase. Nitrides and carbides are formed very early in the preparation of the alloy and constitute the secondary phase. The latter is composed of Niobium, Titanium, Carbon and Nitrogen arranged in a cubic structure mainly found in the matrix and sometimes in interdendritic spaces. This secondary phase constitutes the weakness of the material –sites of crack initiation– because it does not accommodate the deformation and is a source of local stress concentrations. Finally, the  $\delta$  phase has an orthorhombic structure. It forms at the grain boundaries and grows during the heat treatment. This phase has a fine and elongated morphology in the form of needles (Valerio et al., 1994; Azadian et al., 2004; Zhang et al., 2010). It has the essential function of limiting grain growth during heat treatment: Grain boundaries act as barriers to stop dislocation progression during loading. The microstructure used in this work shows a grain size area average around 18  $\mu\text{m}^2$  measured by scanning electron microscope (SEM). In addition no marked crystallographic texture was detected via electron backscatter diffraction (EBSD) observations.

In this work, an Inconel718 forged bar was designed by the manufacturer (Aubert and Duval, 2021). After being heated, melted, and forged, the alloy undergoes a heat treatment. It is first maintained for one hour at around 965°C and then rapidly cooled to room temperature. Then the material is aged in two steps. In the first step, the alloy is held for 8 hours at 720°C and then cooled at a rate of 50°C per hour until reaching 620°C. The second step of the heat treatment is performed by keeping 620°C during 8 hours to be finally cooled in air.

### 3. Experimental procedures

#### 3.1. Specimens and testing conditions

Uni-axial specimens were extracted from a Inconel718 cylindrical bar in the longitudinal direction. Several geometries are chosen in order to be representative of turbine disks loading conditions, this includes: Smooth tensile specimens (ST), notched axisymmetric round bars (NT), flat (D0) and flat notched (D0E) specimens shown in Fig. 1. Mechanical tests have been performed at room temperature and at 500°C for several imposed strain rates from  $10^{-1}$  to  $5.10^{-6} \text{ s}^{-1}$ . Smooth axisymmetric tensile (ST) and notched tensile (NT) specimens are used at both room and high temperatures to identify the viscoplastic behavior of the alloy. Various notch radii for the NT specimens (with a gage length of 10 mm) were designed to obtain different stress triaxiality ratios inside the specimens (Bridgman, 1952). These specimens are introduced to mimick stress concentrators present in the industrial components. Flat tensile (D0) specimens are used to identify the Portevin-Le Chatelier domain from two-dimensional DIC measurements of PLC band propagation. The elongation of the flat specimens (gage length of 15 mm) is measured and the strain rate is calculated using digital image correlation (DIC). A notched flat (D0E) specimen (gage length of 4.5 mm) is used to characterize the appearance and propagation of PLC bands in the case of heterogeneous initial stress distribution.

All tensile tests were performed on a 50 kN load cell MTS hydraulic machine with a lamp oven. The oven is heated to reach 500°C in thirty minutes. The temperature is then hold during another thirty minutes before mechanical testing to ensure an homogeneous temperature inside the specimen. A thermocouple was directly welded on the tested specimens for temperature control. Elongation and diameter reduction were measured using optical method described in (Defaisse et al., 2018) through a furnace window. Finally for D0 and D0E specimens, the strain localization evolution is observed with 2D DIC system. This method provides a good combination of high spatial resolution, a large field of observation, and a relatively high acquisition rate. The strain calculations are performed using Vic-2D software. Image recording is synchronized with the output signal of the testing machine (displacement, load cell and temperature) to ensure accurate measurements. Depending on the strain rate imposed, synchronous image acquisition is performed between 0.1 and 10 frames per second for faster speeds. A 5 Mpx camera is used with a region of interest of 1700×730 pixels.

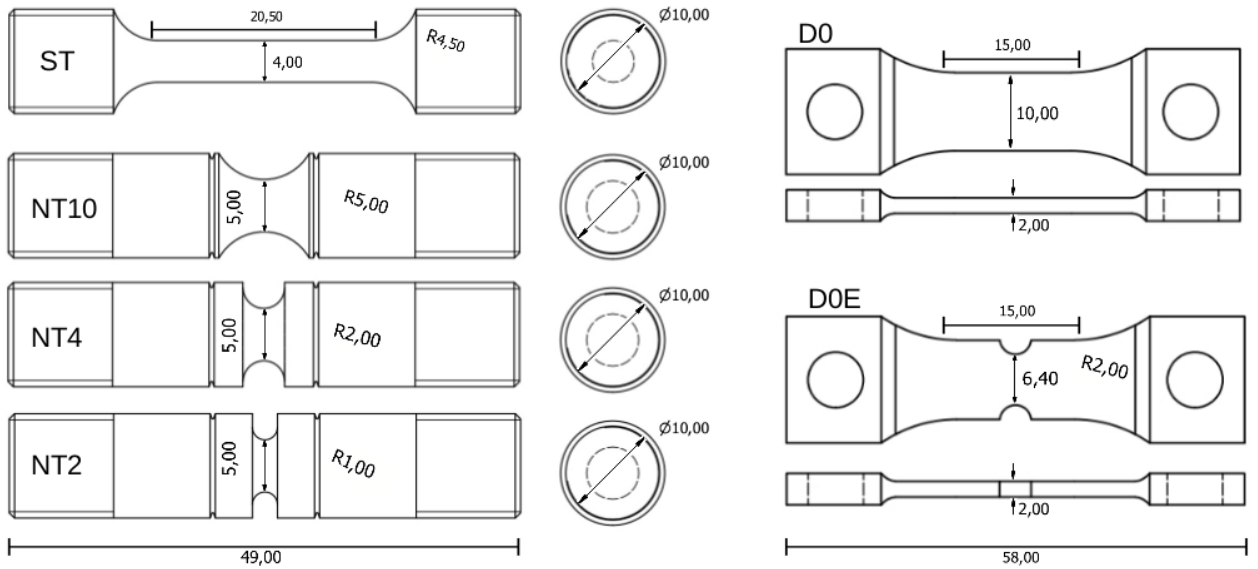


**Figure 1:** Specimen designs used in this work: Smooth (ST) and notched (NT) axisymmetric samples, flat (D0) and flat notched (D0E) tensile specimen geometries. Dimensions are in millimeters.

### 3.2. Engraved speckles for displacement field measurement

Traditionally, the displacement on the surface of a specimen is tracked using either an extensometer placed in direct contact with the specimen, or markers drawn with ink (felt-tip pen, inkjet...), or with colored painting. The disadvantage of using the extensometer is that it is placed at a certain position on the specimen and therefore it does not give access to field measurements. Although the painted markings resolve the insufficiency of the extensometer's measurements, they have weak resistance when the material undergoes large deformations, high temperatures, and/or temperature gradient that cause flaking of the paint making impossible any further displacement measurement.

The proposed solution consists in using neither extensometers nor painted markings but rather a permanent and resistant pattern on the specimen that overcomes the problems described above: Laser engraving process. Two types of markings are exposed in figure 2: i) Points for global displacement tracking and ii) speckle for local displacement tracking. A tool is created to generate an image on which a desired –regular or random– pattern is engraved. In the first case, hatched points of 0.5 mm are laser engraved on the surface at a distance,  $L_0$ , configurable by the user. It corresponds to the initial distance between points and allows to determine the deformation of the interest zone. In the second case an image is reproduced by the laser machine on the surface of the sample. The diameter of the points obtained by laser engraving is between 50 and 80  $\mu\text{m}$  with a random distribution. The distance between two adjacent



points is approximately one to two times the diameter of a point. The size of the engraved image is carried out on a 10×30 mm window in which 5500 to 7000 points are engraved providing a good resolution of the displacement field during post-processing.

This new method has been implemented and tested on all experimental data presented. Many iterations have been carried out to optimize the laser parameters (speed [mm/sec] of the beam, its power [%], its frequency [kHz], its duration [ns], and the number of repetitions of the engraved pattern) to deteriorate the least possible the surface of the material. Fine observations on the local impact of the laser on the material (heating, local remelting of the material) has been realized to optimize the process.

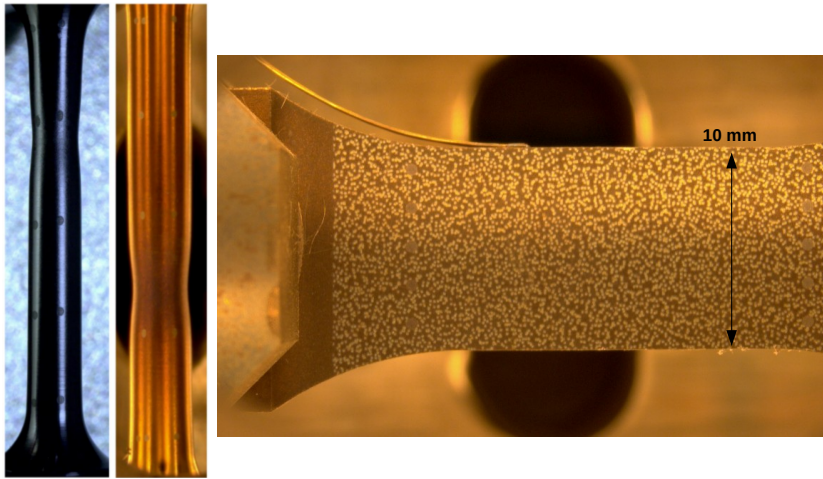


**Figure 2:** Engraved speckles used for displacement measurement by image analysis: i) Large points used at 20°C and 500°C for macroscopic displacement tracking, ii) Refined patterns used at 500°C for microscopic displacement tracking.

This method has the advantage of fully parameterizing the type of speckles according to the targeted application. At the specimen level, this method can be used until fracture of the specimen without to worry about i) the possible indentation of the specimen by the extensometer tips, ii) the deterioration of the extensometer when the specimen breaks. Another example of application would be the monitoring of the initiation and propagation of cracks in a specimen during thermomechanical fatigue loading. At the structural level, this method could be applied on a disk with, on the one hand, a high resolution of points where the stress concentrations are located inducing high strain levels and, on the other hand, a low resolution zone in the center of the disk where deformation is more homogeneous. This method would allow to determine the displacement field at any point of the disk, which is useful to recalibrate the

constitutive model. Another example of application would be to apply a regular pattern in nonvisible areas –typically inside a combustion chamber before its assembly– to measure the deformation of the pattern induced by the thermal loading once the test is completed.

This method proves to be very efficient thanks to the excellent resistance of the pattern at high and very high temperatures despite the oxidation of the material and the large deformations that the material undergoes during the experiments. Moreover, this technique is quick to implement, accurate, repeatable, and easily post-processed with image correlation softwares. In the present study, the speckles do not seem to induce crack initiation in the specimen. No further information is provided since a pending patent is ongoing (Guillermin and Köster, 2021). The question arises whether the surface roughness induced by the speckle preparation may affect the triggering of PLC bands. In one case, the overall tensile curves for two samples with and without surface preparation have been compared, without notable differences in the critical strain and serration amplitude and frequency.

The Green-Lagrange strain measure is computed from the 2D displacement field found by correlation. The strain calculation in Vic-2D is similar to the finite element method algorithm. The input of the strain calculation is a grid of data points. A local mesh of planar triangles is created by connecting these points. The element size is controlled by the step size in the software. The displacement inside a triangular element is obtained by linear approximation (polynomial fit). The displacement gradient is then used for evaluating the Green-Lagrange strain field:

$$\varepsilon_{ij} = \frac{1}{2}(u_{i,j} + u_{j,i} + u_{k,i}u_{k,j}) \quad (1)$$

where  $u_{i,j} = \partial u_i / \partial x_j$  is the Lagrangian gradient of the displacement field here limited to  $i, j \in x, y$ . In addition to the displacement field post-processed on the region of interest, two types of data were extracted: i) The strain as a function of time  $\varepsilon_{yy}(t)$  on the central point, ii) the strain rate on the region of interest defined by  $\dot{\varepsilon}_{yy} = \Delta\varepsilon_{yy} / \Delta t$ . The spatial resolution,  $\Delta x$ , is 18  $\mu\text{m}/\text{pixel}$  for the tests. A subset size of  $40 \times 40$  pixels is used for correlation. The calculation step size (grid point spacing) is 9 pixels. The image acquisition rate during loading depends on the strain rate imposed and varies from  $\Delta t = 0.1$  to 10 s which corresponds to the time between two successive images. In the results presented below the time between two successive images is 0.2 s for D0 and D0E specimens. Throughout this article, the axis  $y$  denotes the tensile axis for all the tests.

#### 4. Constitutive model including dynamic strain aging

The mechanical model used in this work has been introduced by MacCormick (1988) and extended through several works (Zhang et al., 2001; Graff et al., 2004, 2005; Benallal et al., 2006; Böhlke et al., 2009; Mazière et al., 2010a). The constitutive equations are formulated for isotropic nonlinear elastoviscoplastic material behavior. The total strain rate tensor is decomposed into an elastic part and a plastic part:

$$\dot{\underline{\underline{\epsilon}}} = \dot{\underline{\underline{\epsilon}}}^e + \dot{\underline{\underline{\epsilon}}}^p, \quad \dot{\underline{\underline{\epsilon}}}^e = \underline{\underline{\underline{E}}}^{-1} : \dot{\underline{\underline{\sigma}}} \quad (2)$$

where  $\underline{\underline{\underline{E}}}$  is the Hooke fourth order tensor of elastic moduli, and  $\underline{\underline{\underline{E}}}^{-1}$  is its inverse, the elasticity compliance tensor. The evolution of the plastic part is provided by the yield function  $f$  and the plastic flow rule as follows:

$$\dot{\underline{\underline{\epsilon}}}^p = \dot{p} \frac{\partial f}{\partial \underline{\underline{\sigma}}}, \quad f(\underline{\underline{\sigma}}, p, \dot{p}, t_a) = \bar{\sigma} - R(p) - R_a(p, t_a), \quad \dot{p} = R_v^{-1}(f) \quad (3)$$

where  $\dot{p}$  is the viscoplastic multiplier and  $p$  the cumulative plastic strain. The yield function includes an equivalent stress measure according to Hosford (2013):

$$\bar{\sigma} = \left( \frac{1}{2} (|\sigma_I - \sigma_{II}|^n + |\sigma_{II} - \sigma_{III}|^n + |\sigma_{III} - \sigma_I|^n) \right)^{1/n} \quad (4)$$

where  $\sigma_I, \sigma_{II}, \sigma_{III}$  are the principal stresses ranked in the order  $\sigma_I \geq \sigma_{II} \geq \sigma_{III}$ .

The plastic strain hardening function is taken as

$$R(p) = R_0 + \sum_{i=1}^2 Q_i (1 - e^{-b_i p}) \quad (5)$$

where  $R_0$  is the initial yield stress and  $Q_i, b_i$  are material parameters to characterize non-linear isotropic hardening.

The strain rate (viscosity) dependent part in Eq. (3) is chosen in the form of a hyperbolic viscosity function:

$$R_v(\dot{p}) = K \sinh^{-1} \left( \frac{\dot{p}}{\dot{p}_0} \right) \quad (6)$$

The last component of the yield function is the strain aging hardening term  $R_a$ . The contribution  $R_a$  is calculated from the over-concentration  $C$  of solute atoms around dislocations and is a function of the cumulated plastic strain  $p$  and of the aging time variable  $t_a$ .

$$R_a(p, t_a) = P_1 C(p) \left( 1 - \exp \left( - \left( \frac{t_a}{t_o(p)} \right)^\beta \right) \right) = P_1 (c_1 + c_2 p) \left( 1 - \exp \left( - P_2 p^\alpha t_a^\beta \right) \right) \quad (7)$$

The aging time increment is computed from an evolution law in which the cumulated plastic strain rate  $\dot{p}$  intervenes:

$$\dot{t}_a = 1 - \frac{t_a}{w} \dot{p} = 1 - \frac{t_a}{w_1 + w_2 p} \dot{p} \quad (8)$$

The physical meaning of each parameter in Eq. (7) is given in the following:  $P_1 C(p)$  represents the stress resistance to dislocation motion due to the interaction with the solute atoms;  $P_2$  gives the saturation rate of diffusion around dislocations. The aging time  $t_a$  is interpreted as the time required for the concentration of solute atmospheres in the neighborhood of dislocations to reach a critical level and pin the dislocations. The power  $\beta$  is related to the type of diffusion of solute atoms, namely pipe (value of 0.33) or bulk (value of 0.66) diffusion. The parameter  $w$  is linked to the increment of plastic strain carried by the passage of a PLC band. In the original model proposed by McCormick,  $R_a$ , and the waiting time,  $t_0$ , are independent of plastic strain  $p$ . The introduction of such a dependency has been suggested later to improve the model by Zhang et al. (2001) and Böhlke et al. (2009), making use of the functions  $C(p)$ ,  $t_0(p)$  and  $w(p)$ . The previous equations were formulated within the small strain framework. The extension to finite deformation is performed using Jaumann derivative of the stress tensor and additive decomposition of the finite strain rate tensor, see the formulation in (Besson et al., 2009) by means of corotational frames. The finite deformation formulation is used in all finite element simulations of this work.

This model has been implemented in the implicit finite element code Zset<sup>1</sup> (Besson and Foerch, 1997). Global resolution of equilibrium in the static case is solved iteratively by means of a Newton–Raphson method. Time integration of internal variables at Gauss points is performed using an implicit Newton algorithm. Since both internal variables, namely the cumulative plastic strain  $p$  and the aging time  $t_a$ , may undergo large local increments, the global solution convergence usually requires very small time steps. In the case of divergence of the Newton–Raphson iterations, Mazière et al. (2010a) proposed a mixed integration algorithm combining explicit (Runge–Kutta) and implicit  $\Theta$ -integration methods, associated with automatic control of time stepping. At the beginning of each global time increment, the integration of the behavior law is performed on each integration point using  $\Theta$ -method. When strain localization phenomena take place, such as propagating bands of plastic strain rate, local divergences may occur. The integration of constitutive equations switches then from the implicit Euler to an explicit fourth-order Runge–Kutta method with automatic time-substepping.

---

<sup>1</sup><http://www.zset-software.com>

## 5. Identification strategy of the viscoplastic constitutive laws

The methodology for the identification of the material parameters present in the constitutive model described in the previous section is summarized in Fig. 3, and detailed in the following sub-sections. The identification is performed at two temperatures: Room temperature and 500°C. To determine the behavior law of Inconel718 at room temperature, two steps are required and are represented in the black boxes of Fig. 3. The hardening laws and the plastic yield criterion are first identified based on the experimental stress-strain responses of all the geometries exposed in section 3.1 using an optimization strategy. The latter is based on the determination of a quadratic cost function evaluating the difference between the experimental results and the results of finite element simulations for the various specimen. Second, the viscosity parameters are calibrated on ST specimens for two different imposed strain rates. The identification of the McCormick model parameters at 500°C is divided into three steps that are represented in the red blocks of Fig. 3. The response of D0 specimens tested at several imposed strain rates is used to first reproduce the negative strain rate sensitivity using only simulations at the material point level assuming homogeneous deformation. The prediction of the critical plastic strain for the occurrence of PLC instabilities is performed using the bifurcation analysis proposed in the works (Mazière and Dierke, 2012; Ren et al., 2017). Third, the strain carried by the PLC bands measured by DIC is used for the determination of remaining parameters. Due to the computation cost of full 3D simulations of PLC band propagation, this step is based on a 3D coarse mesh plate with the same gage-length as the D0 specimen. The validation step is detailed in section 6, where all the geometries are compared to full 3D simulations with sufficiently fine mesh size. Mesh refinement leads to thinner PLC bands and higher plastic strain rate inside the bands, as documented in the literature (Mazière et al., 2010).

### 5.1. Plastic behavior and positive strain rate sensitivity at 20°C

An inverse method is used to identify the hardening law parameters, the plastic criterion, and the positive strain rate sensitivity. Considering all the specimens in the database, the cost function of the optimization is constructed as a sum of two terms. The first term, which is used only for ST specimen before necking, is based on the quadratic difference between experimental and simulated longitudinal elongation between two points before necking. The second term, which is used for NT specimen, is based on the quadratic difference between experimental and simulated results on the cross section reduction measurement until fracture of the sample. To compare experimental points at a same time

### Portevin-Le Chatelier effect in a nickel-base superalloy for turbine disks

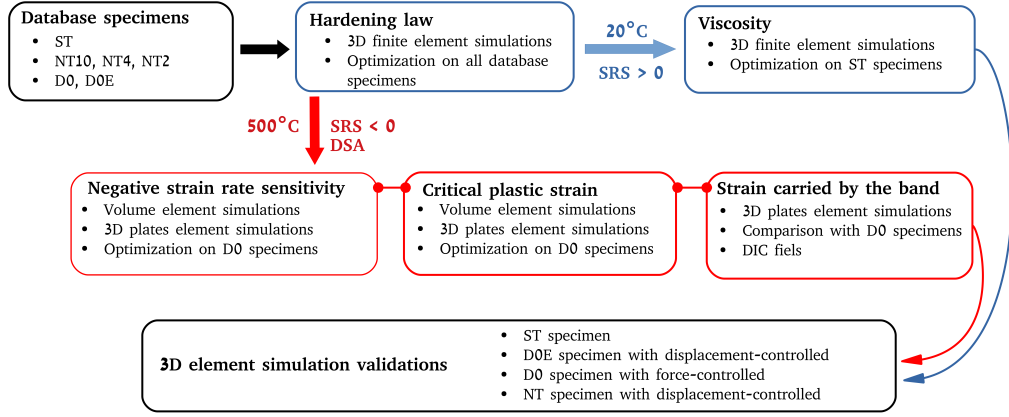


**Figure 3:** Summary of the identification strategy scheme of the constitutive model at two temperatures.

with simulation points, the simulated curves are interpolated at the corresponding experimental point. The trapeze rule integration is used so that the cost function is independent from the number of acquired data points. Finally weight coefficients are introduced to equally divide the contribution of the two terms in the cost function and also equally between all the specimens. The goal of the optimization is to minimize the global function  $\xi$  which corresponds to all specimens tested and simulated of the database.

$$\xi = \sum_0^n \omega_n \left\{ \int_0^{\frac{\Delta L}{L_0} \Big|_{Necking}} \left[ F_{exp} \left( \frac{\Delta L}{L_0} \Big|_{exp} \right) - F_{sim} \left( \frac{\Delta L}{L_0} \Big|_{sim} \right) \right]^2 d\varepsilon + \int_0^{\frac{\Delta \Phi}{\Phi_0} \Big|_{Fracture}} \left[ F_{exp} \left( \frac{\Delta \Phi}{\Phi_0} \Big|_{exp} \right) - F_{sim} \left( \frac{\Delta \Phi}{\Phi_0} \Big|_{sim} \right) \right]^2 d \frac{\Delta \Phi}{\Phi_0} \right\} \quad (9)$$

Regarding the Hosford yield function (4), the isotropic hardening law (5), and the viscoplastic flow rule (6), the optimization is carried out with respect to the 8 corresponding parameters using the Levenberg-Marquardt algorithm (Levenberg, 1944). The retained parameter values lie in the expected physical range of validity and the simulations with optimized parameters reproduce well the experimental results. The calibrated plasticity model is shown in Fig. 4 and 5 for all database specimens, with satisfactory agreement between simulation and experiment in terms of stress/strain curves. It can be noticed that ST and D0 specimens give the same behavior response. The found parameters characterizing the behavior at room temperature are given in Table 2.

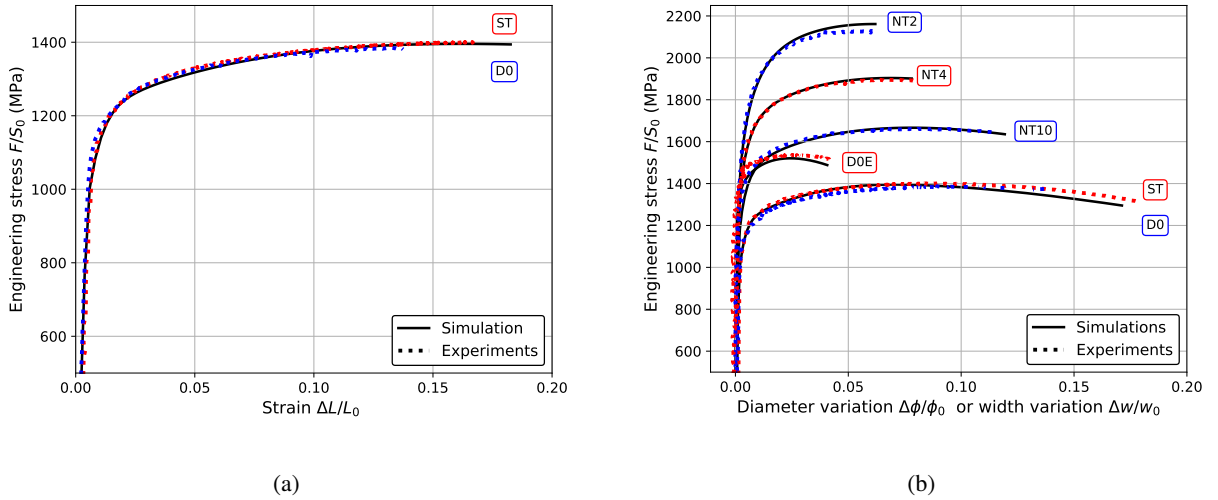


**Figure 4:** Plastic behavior identified using finite element simulations for all samples tested at 20°C: a) Engineering stress vs. elongation (comparison is performed up to necking); b) Engineering stress vs. diameter variation or width variation (comparison is performed up to fracture).

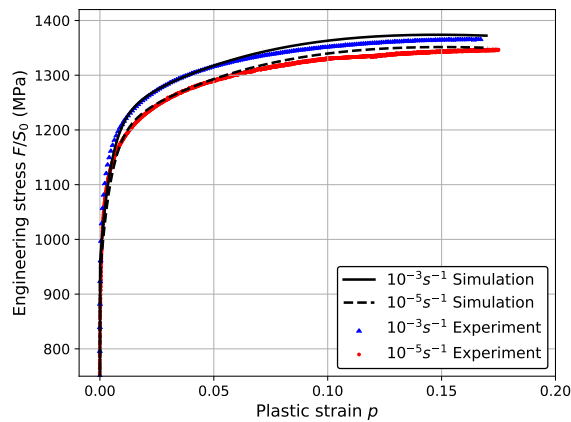


**Figure 5:** Viscoplastic behavior identified using finite element simulations for ST sample tested at 20°C. Engineering stress vs. plastic strain.

## 5.2. Negative strain rate sensitivity at 500°C

For aged treated Inconel718, it is found that dynamic strain aging effects can occur in the temperature range from 200°C to 700°C and strain rate domain from  $10^{-7} s^{-1}$  to  $10^{-2} s^{-1}$ , in the form of serrated stress-strain curves observed by (Hale et al., 2001; Garat et al., 2008; Prasad et al., 2010). Portevin-Le Chatelier instabilities appear when the negative sensitivity of the stress to the strain rate takes over the positive strain hardening sensitivity (Kubin and Estrin,

**Table 2**

Hardening law and viscosity parameters obtained for Inconel718 at room temperature.

| $R_0$ | $Q_1$ | $b_1$ | $Q_2$ | $b_2$ | $\dot{p}_0$ | $K$  | $n$ |
|-------|-------|-------|-------|-------|-------------|------|-----|
| (MPa) | (MPa) | -     | (MPa) | -     | $s^{-1}$    | MPa  | -   |
| 894   | 256   | 215   | 579   | 7.37  | $10^{-8}$   | 5.67 | 8   |

1991). The first step to calibrate the model parameters is to numerically reproduce the experimental negative strain rate sensitivity visible in Fig. 6a. For this purpose, the stress values simulated for given strain rate and plastic strain level are simulated (material point simulation) and optimized w.r.t. experimental values, as shown in Fig. 6b. Four plastic strain levels were chosen. To avoid inconsistent values because of serrations, the experimental stresses are taken as averages over a small window of plastic strain (0.001). The negative strain rate sensitivity at 500°C is clearly visible in the investigated range of strain rates from  $5 \cdot 10^{-6} s^{-1}$  to  $10^{-1} s^{-1}$ . The boundaries of the domain of negative strain rate sensitivity are also visible since the stress values reach a plateau at low and high strain rates, the left plateau being higher than the right one in Fig. 6b.

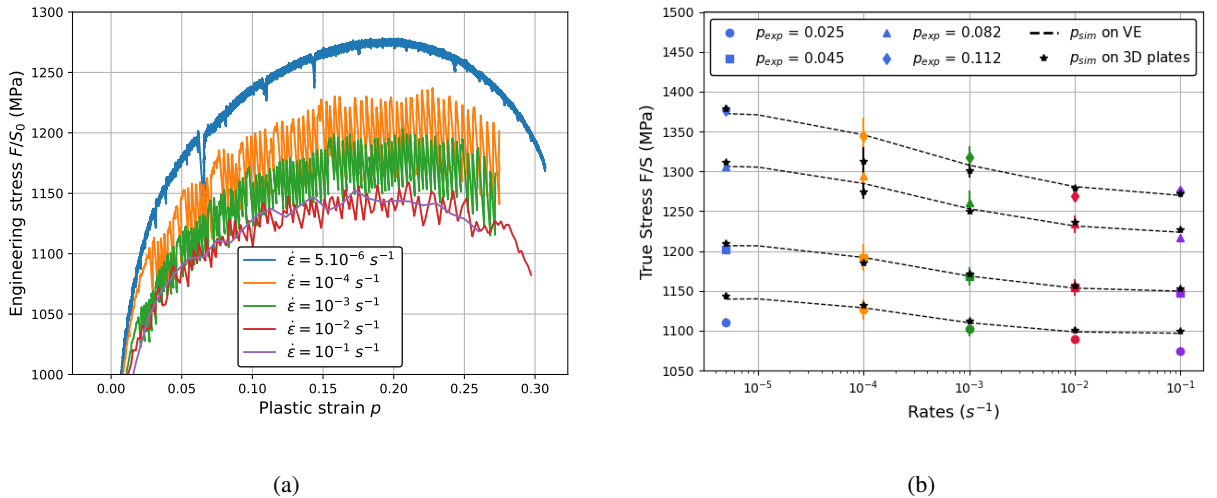


**Figure 6:** Experimental results on D0 specimens for all tested strain rates [ $5 \cdot 10^{-6} s^{-1}$ ,  $10^{-1} s^{-1}$ ]: a) Engineering stress vs. plastic strain; b) True stress vs. total strain rate for different plastic strain levels. Solid points represent mean values of the experimental true stress on a plastic strain interval  $p_{exp} \pm 0.001$  around value  $p_{exp}$ . The error bars represent the standard deviation on this domain. Volume element simulations are shown with dashlines and black stars for 3D plate finite element simulations.



### 5.3. Bifurcation analysis

The critical condition for the occurrence of serrations (PLC effect) during tensile test can be predicted by a theoretical analysis. This analysis is carried out to better calibrate the model parameters according to experimental data. It consists in introducing a small exponential perturbation in the set of evolution equations for internal variables, assuming that the solution can be written as a multiplication form of the product between space  $x$  and time  $t$ :

$$\delta[\mathbf{X}(x, t)] = [\mathbf{X}_0(x)] \exp(\lambda t) = \begin{bmatrix} \delta p \\ \delta t_a \\ \delta \sigma \end{bmatrix} \quad (10)$$

The  $\lambda$  parameter is related to the growth (or decay) of the perturbation and to the shape of its evolution (oscillating or hyperbolic). This perturbation is introduced in the constitutive one-dimensional equation for simple tension at prescribed plastic strain rate:

$$\delta \sigma = \frac{dR(p)}{dp} \delta p + \frac{\partial R_a(p, t_a)}{\partial p} \delta p + \frac{\partial R_a(p, t_a)}{\partial t_a} \delta t_a + \frac{dR_v(\dot{p})}{d\dot{p}} \delta \dot{p} \quad (11)$$

The analysis is carried out following the method presented in (Mazière and Dierke, 2012; Ren et al., 2017). The small strain assumption is adopted for simplicity in this section. The growth of the perturbation is studied through a spectral analysis of the 2x2 transfer matrix  $\mathbf{M}$  which relates the perturbation of internal variables to the perturbation of their rates:

$$\begin{bmatrix} \delta \dot{p} \\ \delta \dot{t}_a \end{bmatrix} = \left( \frac{dR_v(\dot{p})}{d\dot{p}} \right)^{-1} \begin{bmatrix} \sigma - \frac{dR(p)}{dp} - \frac{\partial R_a(p, t_a)}{\partial p} & -\frac{\partial R_a(p, t_a)}{\partial t_a} \\ \frac{t_a}{w} \left( \frac{dR(p)}{dp} + \frac{\partial R_a(p, t_a)}{\partial p} - \sigma \right) + \frac{t_a \dot{p} w_2}{w^2} \frac{dR_v}{d\dot{p}} & -\frac{1}{w} \left( \dot{p} \frac{dR_v(\dot{p})}{d\dot{p}} - t_a \frac{\partial R_a(p, t_a)}{\partial t_a} \right) \end{bmatrix} \begin{bmatrix} \delta p \\ \delta t_a \end{bmatrix} \quad (12)$$

$$\begin{bmatrix} \delta \dot{p} \\ \delta \dot{t}_a \end{bmatrix} = \mathbf{M} \begin{bmatrix} \delta p \\ \delta t_a \end{bmatrix} \quad (13)$$

The trace of  $\mathbf{M}$ , its determinant, and its two eigenvalues can be successively computed. Mazière and Dierke (2012) showed that the appropriate criterion for the occurrence of the PLC effect is the possibility of exponential growth. This approach was validated on material model and parameters from (Böhlke et al., 2009) for an Al-Cu alloy and from (Ren et al., 2017) for a C-Mn steel material. Exponential growth of the perturbation corresponds to real and positive eigenvalues of the matrix  $\mathbf{M}$ . This requires  $\text{Trace}(\mathbf{M}) > 0$  and  $(\text{Trace}(\mathbf{M}))^2 - 4 \det(\mathbf{M}) > 0$ . This criterion is evaluated

for each applied strain rate, thus giving the critical plastic strain at which serrations start. The evolution of the critical plastic strain vs. the strain rate is represented by the U-shape curve of Fig. 7a.

According to the model chosen in section 4, a sensitivity study of model parameters on the influence of the U-shape curve has been performed. Considering the saturated value of the aging time

$$t_a^\infty = \frac{w}{\dot{p}} \quad (14)$$

obtained from Eq. (8) by setting  $\dot{\epsilon}_a = 0$ , the U-shape curve is determined analytically over the studied strain rate range, see figure 7a. The role of each parameter on the shape of the curve is shown in this figure. The increase of  $c_1$  leads to a vertical translation of the U-shaped curve towards lower critical plastic strain values, whereas the viscosity parameter  $K$  has the opposite effect with in addition a closing of the two branches of the curve. The increase of  $P_2$  translates the U-curve horizontally towards higher strain rates. On the other hand, the increase of the parameter  $w_1$  translates the U-curve on both vertical and horizontal axes towards higher critical plastic strain and strain rates. Increasing  $c_2$  widens the bottom of the U-curve and thus increases the PLC domain over a larger range of strain rates. Finally the parameters  $\alpha$  and  $w_2$  affect the left branch of the curve allowing to control the occurrence or not of the PLC effect at for low strain rates.

In addition to the negative strain rate sensitivity previously detailed in section 5.2, the experimental critical plastic strain for PLC has also been identified experimentally and taken into account in the parameter identification as weighted term in the cost function to be minimized. Each experimental critical plastic strain (green circle) is plotted in figure 7b and compared first to the analytical model (black dotted line), second to volume element simulations (red triangles), and finally to finite element simulations of 3D plates (blue stars). Three-dimensional full plates representative of the central zone of D0 specimen ( $15 \times 10$  mm) are used to calibrate the increment of deformation inside the band. The plates are meshed with quadratic hexahedral elements (c3d20r) with limited total number of degrees of freedom (360 elements, 2049 nodes) to get faster calculations than for the D0 geometry. A uniform prescribed vertical displacement is applied to the bottom of the plate whereas the top of the plate is clamped in the same direction with additional conditions to avoid the rigid body displacement. It is worth underlining that the model with the set of obtained parameters reproduces well the experimental critical plastic strain except for the lowest strain rate. However, the macroscopic blue curve of Fig. 6a, representing the lowest strain rate, shows one or two serrations as opposed to the large number of serrations for

higher imposed strain rates. The end of the PLC domain is therefore very close. The validity of the critical plastic strain of the lowest strain rate, in the sense of occurrence or not of the PLC effect at a given plastic strain, is questionable and it was decided to shift the critical value of the plastic strain to a higher value on the U-shaped curve.

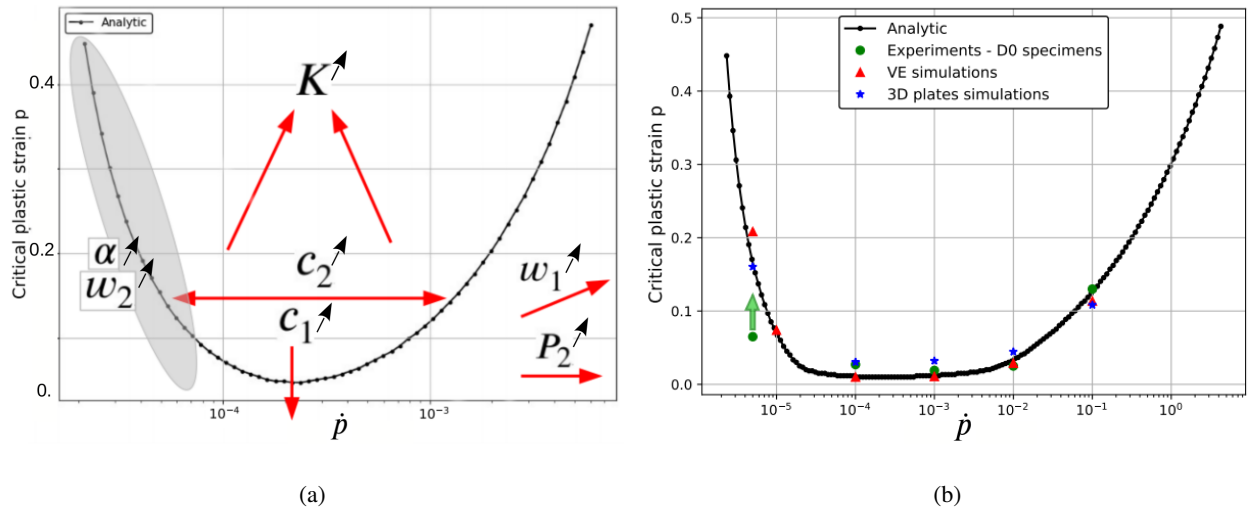


**Figure 7:** Both curves are representing critical plastic strain for PLC vs. plastic strain rate values: a) Schematic curve with the qualitative influence of the increase of each parameter on the curve shape; b) Comparison between the predicted analytical curve identified with parameters calibrated from experimental data, volume element simulations and plates 3D finite element simulations.

#### 5.4. Strain carried by the band

Few works can be found in the literature providing local fields measurements carried out on a nickel-based superalloy at 500°C, except (Swaminathan et al., 2015; Cai et al., 2017). The method described in section 3.2 has been applied to access to the local field of the displacement on the flat specimens (D0 and D0E). During these experiments, oxidation was detected only for low strain rates and no glowing was observed so that accurate strain field measurements were possible.

Figure 8a shows the strain experienced by a middle point on the zone of interest of a D0 specimen as a function of time for two distinct strain rates. The steps on the curve represent the strain increment carried by the bands that propagate through the sample. These strain values increase when the imposed strain rate decreases. For a strain rate of  $10^{-2} \text{ s}^{-1}$ , the mean strain carried by the bands during the experiment is 0.0078, whereas for lower strain rates  $10^{-3} \text{ s}^{-1}$  and  $10^{-4} \text{ s}^{-1}$ , the mean strain carried by a band is respectively 0.0111 and 0.0157. On the other hand, the strain rate

field in the region of interest at various time steps is displayed in Fig. 8b. This field reveals the existence of type A PLC bands. The strain rate inside the band is found to increase during the experiment. The maximum strain rate in the middle of the band at the end of the experiment is about 10 times the value of the imposed strain rate. Bands appear and disappear with an angle of roughly  $55^\circ$  from the tensile axis. As the purpose of this study is not to observe in details the propagation of bands in the interest zone, the frequency of image acquisition previously chosen was not sufficiently high to accurately follow their propagation.

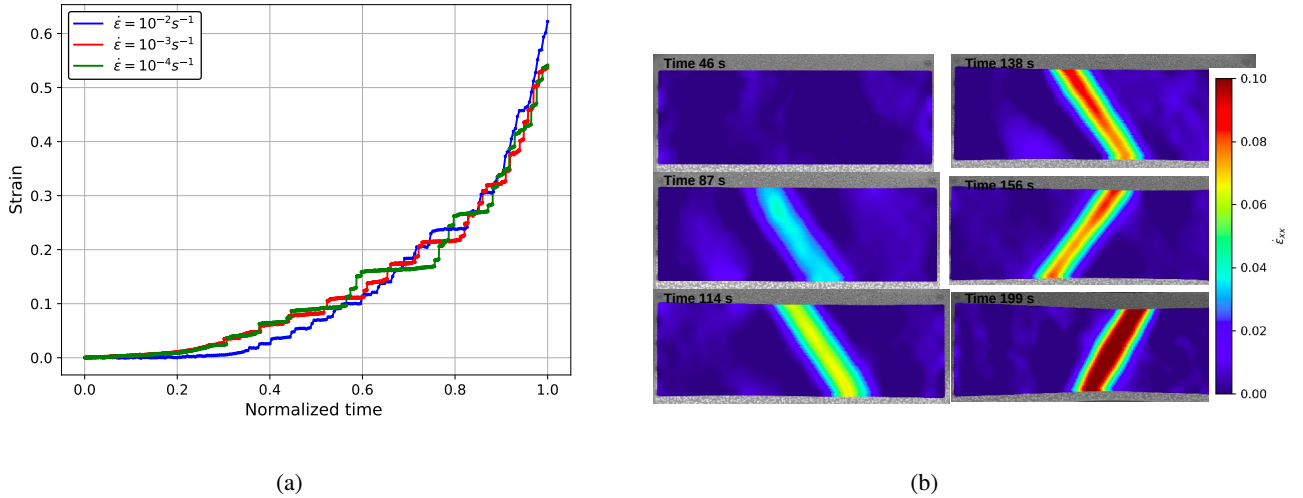


**Figure 8:** Results of local strain field measurements with DIC on D0 specimens: a) Strain vs. time of the center point of the specimen for three imposed strain rates; b) Strain rate field in the region of interest for an imposed strain rate of  $10^{-3} \text{ s}^{-1}$ .

To improve the calibration of the model, the increment of plastic strain carried by the bands has been used to optimize the  $w_1$  parameter, see Eq. (8). For this purpose, 3D simulations on plates with the same dimensions of the D0 specimen interest zone have been carried out. A coarse mesh with quadratic hexahedral and reduced integration (c3d20r) elements is used (figure 9b). The coarse mesh allows for fast enough simulations to be involved in the identification procedure. It is clearly established that the parameter  $w_1$  plays an important role in the strain increment transported by the band. The higher the parameter  $w_1$ , the higher the steps in figure 9a. The curves have been translated along the  $y$ -axis for better visibility. Once the value of  $w_1$  is determined according to experimental strain carried by the bands measured by DIC, the critical plastic strain associated with each imposed strain rate is plotted in Fig. 7b. The obtained results are in agreement with those performed on volume elements and those given by the analytical

bifurcation analysis.

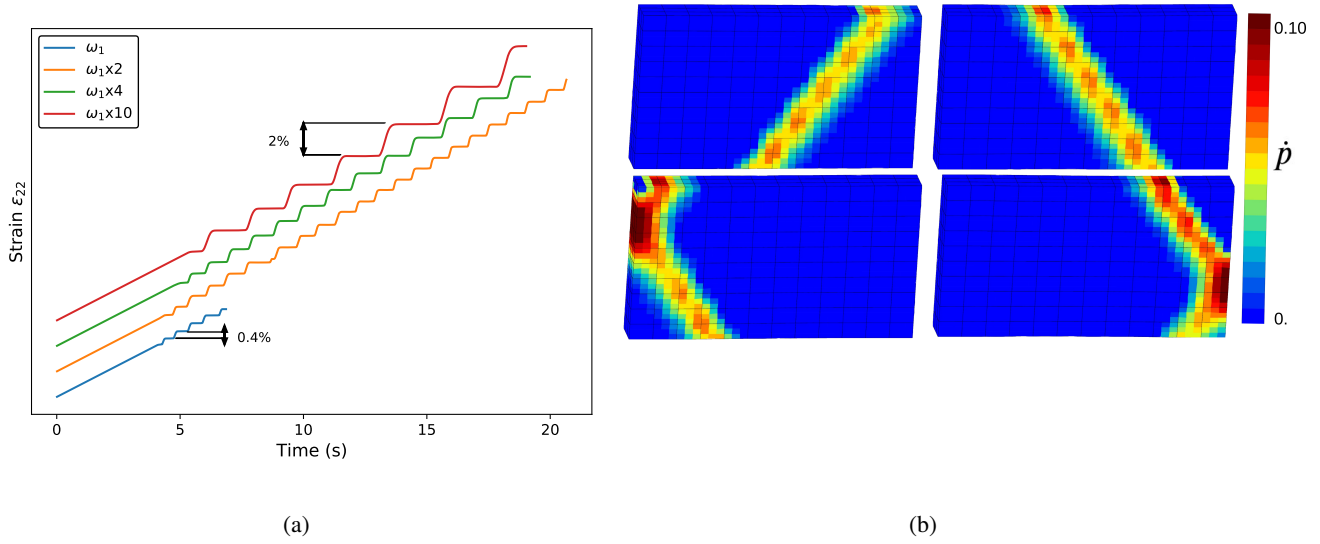


**Figure 9:** 3D plate finite element simulations for a strain rate of  $10^{-3} \text{ s}^{-1}$ : a) Sensitivity study w.r.t.  $\omega_1$  parameter. Strain vs. time at the center point with curves translated for better reading, b) Strain rate field at different plastic strain levels.

The material parameters taking into account the whole identification strategy detailed previously are gathered in Table 3. The identification of this viscoplastic model takes into account a reliable transcription of i) the negative sensitivity of the strain rate to the flow stress, ii) the critical plastic strain which is a good predictor of the instability detection, and iii) the plastic strain increment in the band.

**Table 3**

Identified McCormick model parameters for Inconel718 at  $500^\circ\text{C}$ .

| $R_0$  | $P_1$ | $P_2$               | $c_1$  | $c_2$  | $\alpha_p$ | $\beta$ | $\omega_1$           | $\omega_2$ |
|--------|-------|---------------------|--------|--------|------------|---------|----------------------|------------|
| (MPa)  | (MPa) | ( $\text{s}^{-1}$ ) | -      | -      | -          | -       | -                    | -          |
| 684.00 | 1.00  | 1.15                | 102.00 | 878.00 | 0.00       | 0.33    | $1.45 \cdot 10^{-4}$ | $10^{-5}$  |

## 6. Validation on actual specimen geometries

Once satisfactory results were obtained regarding the comparison between simulated and experimental data for D0 specimens, as done in section 5, a validation on several other specimen geometries has been performed. The

experiments were performed at 500°C, under displacement or force control. The behavior law uses the parameters listed in table 3. As the bands break the geometrical symmetry of the specimen, full 3D specimens are meshed with quadratic hexahedral elements (c3d20r). The macroscopic simulated curves are superimposed on the experimental curves using strain values measured over the same gage-length. Several specimen geometries are investigated in the following subsections.

### 6.1. Axi-symmetric specimen under displacement control

The first model validation has been performed for an axi-symmetric ST specimen under displacement control with a strain rate of  $10^{-3} \text{ s}^{-1}$  (Fig. 10a). Numerical results give access to the evolution of each constitutive variable during the occurrence of the PLC phenomenon, see Fig. 10b for the fields of cumulative plastic strain, plastic strain rate, concentration of solute atoms and aging time. During the elastic stage, the solute atom concentration and the aging time increase. At the end of the elastic rise, these two variables become heterogeneous at both fillets that become initiation sites for the PLC bands. Depending on the imposed strain rate, the bands appear either in the top fillet or in the bottom, or in both. In this simulation the band selects the bottom of the sample before propagating due to numerical instabilities. The plastic strain rate which was null during the elastic stage becomes heterogeneous in the zone of interest. Once a band is formed, the solute atoms that had pinned the forest of dislocations rearrange. This explains that atom concentration decreases at the place where the band was produced (Fig. 10b). However in front of the band the atom concentration increases explaining microscopically the fact that solute atoms diffuse to the next forest of dislocations. The aging time decreases in front of the previously formed band, thus causing its propagation in the specimen. Finally, the phenomenon repeats itself dynamically until the maximal load or the fracture of the specimen as long as the imposed strain rate and the temperature remain in the PLC domain.

Fig. 10b presents the simulated fields at a given time marked -1- on the macroscopic curve in Fig. 10a. In addition, the right image in figure 10b presents the strain rate on the cross-sectional view of the specimen on which the conical shape of the band can be observed. Geometrically, the tip of the red cone corresponds to the lower part of the band and propagates in the direction of the base of the red cone. The band propagation can be observed in Fig. 11 in the time interval represented by the blue arrows in Fig. 10a. Fig. 11 shows that the visible stress drop on the macroscopic curve of figure 10a corresponds to the fact that the band reaches the top or the bottom of the specimen and thus the band

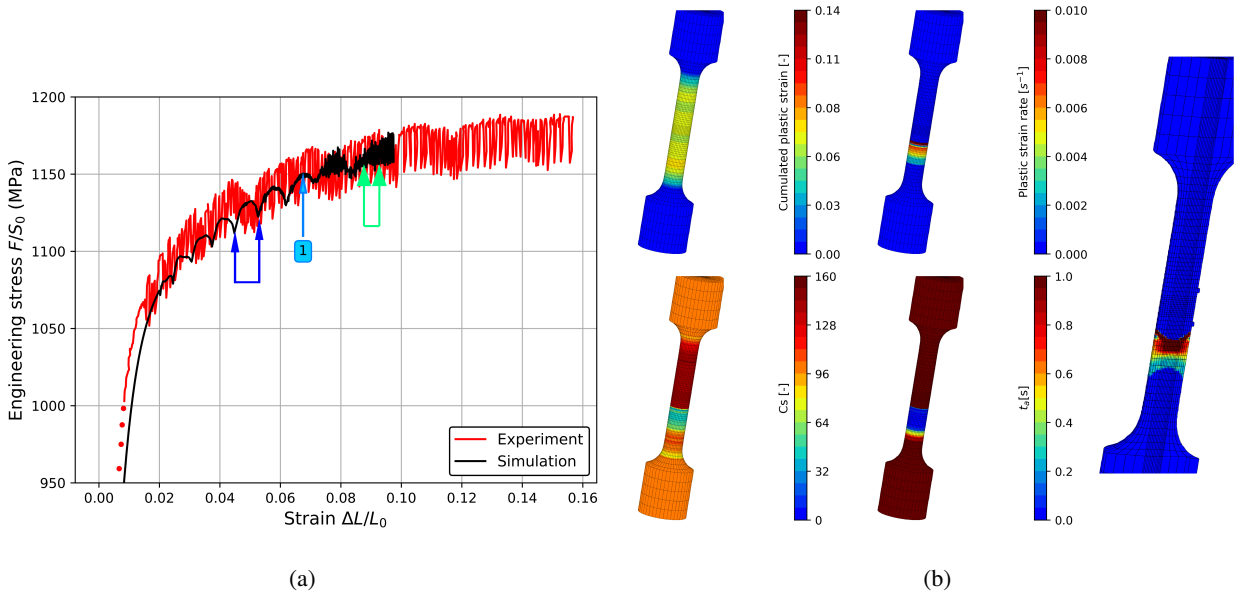


**Figure 10:** Displacement-controlled test on ST specimen at 500°C with an imposed strain rate of  $10^{-3}s^{-1}$ : a) Comparison between experimental results and finite element simulation for the stress vs. strain curve; b) Simulation results at one strain level with associated internal variables.

propagation changes direction. During this stage, the strain rate increases and reaches its maximum value at one end of the specimen before the band changes direction. It decreases by a factor of three before increasing again during the propagation of the band. Starting from a strain level of about 0.07, the frequency of serrations significantly increases on the macroscopic curve in figure 10a. The first part of the macroscopic curve is in good agreement with type A of PLC band and corresponds in Fig. 11 to a steady propagation of the band between the top and the bottom of the specimen. However at a given time of the simulation the frequency of serrations increases causing a more chaotic propagation as it is explicitly showed in Fig. 12. The transition from type A to type B occurs with a more intermittent propagation. Several morphology of serrations (A,B,C) exist and are well known in the literature (Strudel, 1979; Amokhtar et al., 2006; Ranc and Wagner, 2008).

## 6.2. DOE specimen under displacement control

A second validation of the model is presented for the flat notched geometry (DOE) with a strain rate of  $10^{-3}s^{-1}$  under displacement control. In addition 2D correlation measurements were made using the pattern method explained in section 3.2. One can notice in Fig. 13a that serrations occur at the beginning of the plastic flow and are well predicted

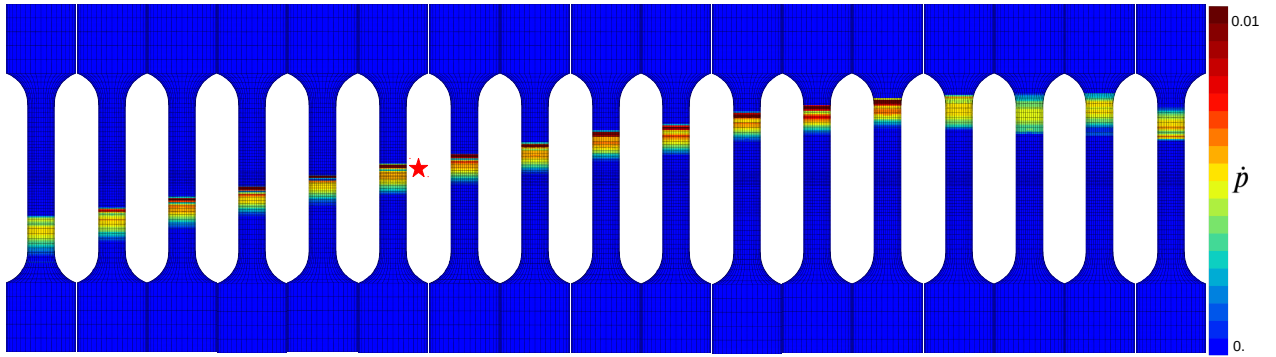


**Figure 11:** Simulation results of the plastic strain rate ( $s^{-1}$ ) between the two times represented by blue arrows in figure 10a. The red star corresponds to the time when the maximum of load between the two blue arrows is reached.

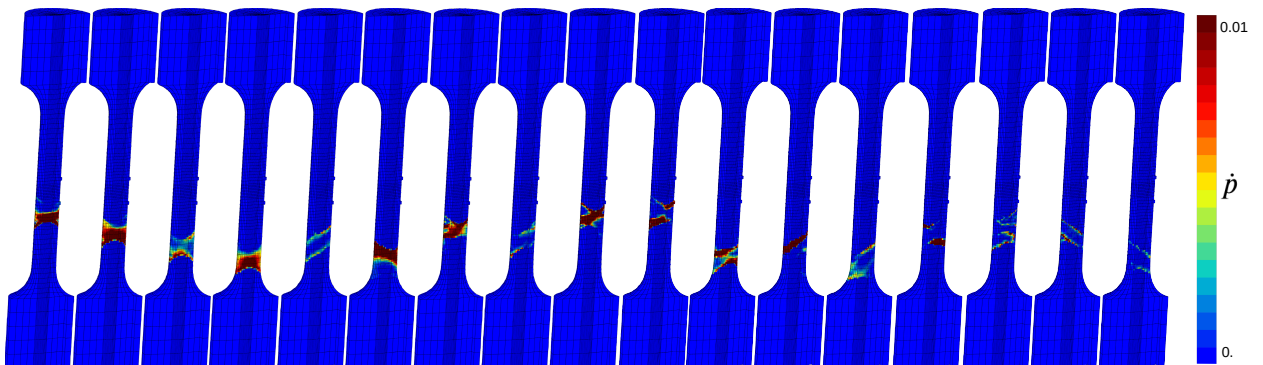


**Figure 12:** Simulation results of the plastic strain rate ( $s^{-1}$ ) between the two times represented by green arrows in figure 10a. The cross-sectional view of the specimen shows the evolution of the initial shape of the cone in figure 11 to more complex band shape.

by the numerical model.

Deformation bands are mainly oriented horizontally in the minimal cross-section of the specimen, see Fig. 13b. At the loading stages 1 and 3, the bands moving up (or down) are slightly curved. Even though the band crosses the specimen from the left to the right, the strain rate seems higher on one side than on the other, for instance in Fig. 13b, stage 6, where the right notch point experiences a higher strain rate than the left side. This phenomenon has also been observed in the simulated fields of Fig. 14). The simulation reveals that after the band appears on one side and crosses the entire section of the specimen, it propagates in the upper or lower part of the specimen and does not remain totally confined in the minimal cross section. It can be observed that even if the morphology of the bands is similar between experimental results and simulated field, the value of the plastic strain rate obtained by simulation seems to be higher.



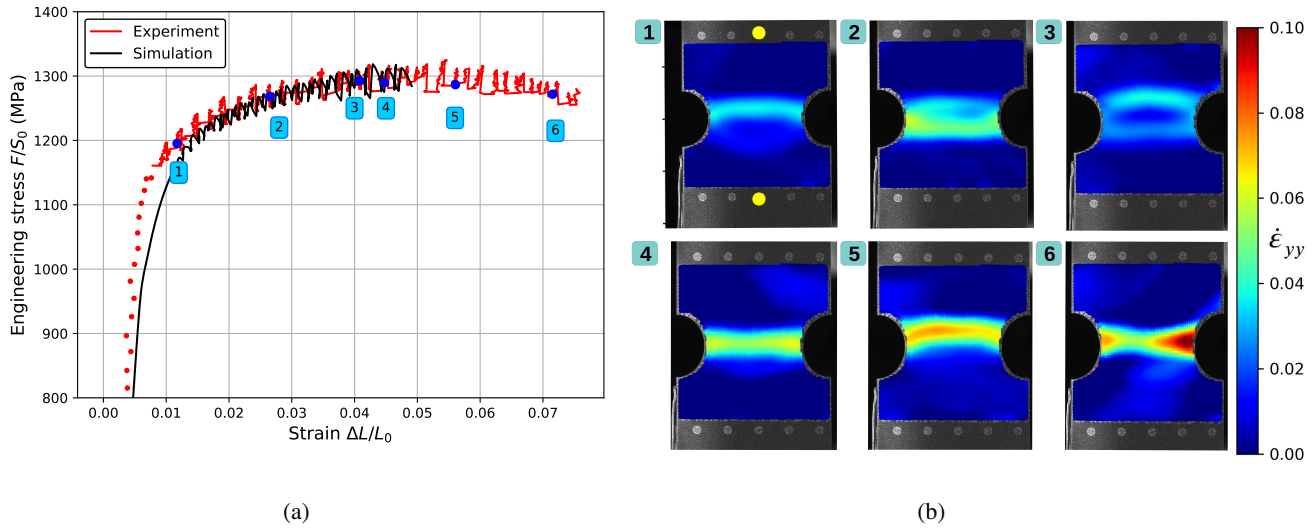


**Figure 13:** Displacement-controlled test on D0E specimen at 500°C: a) Comparison between experimental and finite element simulation for the stress vs. strain curve; b) DIC results for the strain rate fields ( $s^{-1}$ ) at six different strain levels. The two yellow points in the image 1 correspond to the virtual extensometry basis.

It has been checked on the finite element simulation that the total strain rate in the loading direction is very close to the plastic strain rate. In Fig. 14, three maps corresponding to successive simulation steps are presented around the same time step as in the experiment. No direct quantitative comparison between experimental and simulation strain rate maps is possible at a given loading time due to the random character of PLC band formation and propagation.

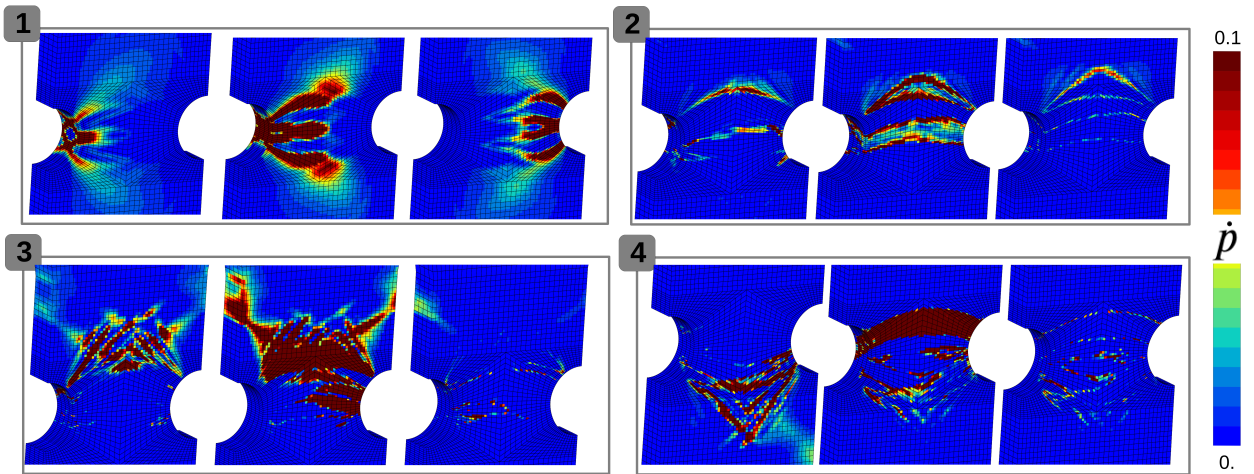
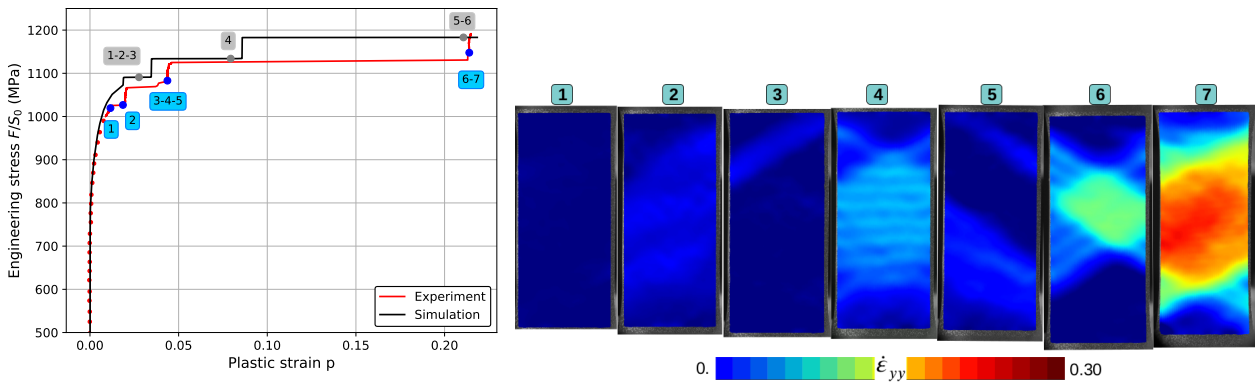


**Figure 14:** Simulation of the plastic strain rate fields at different times represented in figure 13a.

### 6.3. D0 specimen under force control

The objective of this work is to better predict the burst speed of turbine discs for helicopter turboshaft engines. As these disks are loaded in rotational speed, an experimental force-controlled test was carried out at 500°C. By imposing a force rate of  $0.05 \text{ kN}\cdot\text{s}^{-1}$ , corresponding to a stress rate of  $2.5 \text{ MPa}\cdot\text{s}^{-1}$ , DSA still occurs causing three plateaus on the stress-strain curve in Fig. 15a. It is known in the literature that the shape of the stress-strain curve depends on the type of testing machine (Bodner, 1967; Cuddy and Leslie, 1972; Yamasaki et al., 2021). For stiff machines, both ends of the specimen are fixed, therefore when the instantaneous strain of the specimen exceeds the crosshead speed, the load decreases. In contrast, when soft machines are used, a staircase-shape stress-strain curve is obtained. Under load-controlled testing, the machine behaves as an infinitely soft machine producing steps as observed in Fig. 15a.



(a)

(b)

**Figure 15:** Force-controlled test on D0 specimen at 500°C: a) Comparison between experimental results and finite element simulation for the stress vs. strain curve; b) DIC results for strain rate fields at seven different plastic strain levels (unit  $\text{s}^{-1}$ ).

The amplitude of strain carried by the successive bands increases considerably starting with strain jumps from 0.001 to more than 0.15 for the last band. During each plateau, the strain rate in the band increases (a band is propagating) and decreases due to the work hardening to become equal to the elastic strain rate during the rising phases of the curve. DIC measurements of Fig. 15b show that each plateau on the stress–plastic strain curves corresponds to the occurrence of a strain burst in the form of a rapidly propagating strain localisation band through the sample. The morphology of the band is very different from the one obtained on the same geometry in displacement control (see Fig. 8b). In this

case the band is diffused in all the specimen as opposed to localized thin bands occurring in displacement controlled testing. Results obtained with a 3D simulation seem to be in good agreement with the experiment. In Fig. 15a, the predicted critical plastic strain is slightly larger than on the experimental curve. The strain levels of the next plateaus well represent the strain jumps observed in the experiment. It must be noted that the occurrence of each strain burst is an instability displaying stochastic features so that there is no point in trying to predict the exact position of each plateau on the stress-strain curve. The model predicts rather accurately, in a statistical sense, the time series of burst and the mean amplitude of strain jumps. Finally, the simulated plastic strain rate fields in Fig. 16 are in agreement with the measured DIC fields of Fig. 15b.

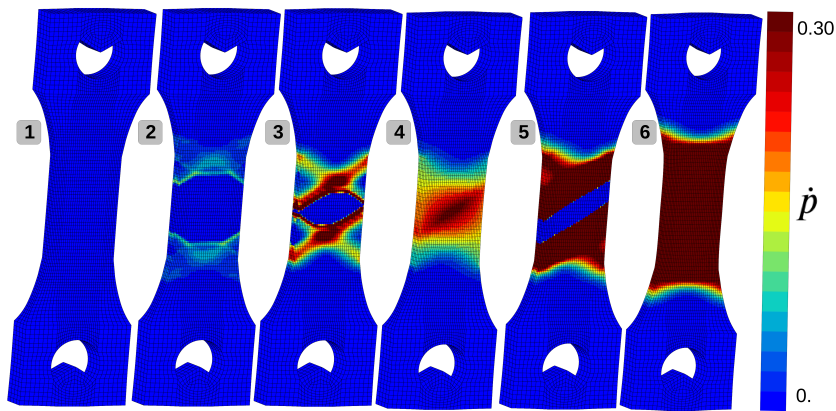


**Figure 16:** 3D simulation results on D0 specimen under force-controlled loading conditions. Plastic strain rate ( $s^{-1}$ ) field at six different strain levels corresponding to the grey numbers 1 to 6 indicated in the stress-strain curve of Fig. 15a.

#### 6.4. Axi-symmetric notched specimens under displacement control

The last validation of the model is done on the three axi-symmetric notched (NT) specimens under displacement-control. The strain rate imposed to the three geometries is  $10^{-3} s^{-1}$  which corresponds to a displacement of  $0.009 mm.s^{-1}$  for NT10,  $0.004 mm.s^{-1}$  for NT4, and,  $0.002 mm.s^{-1}$  for NT2. The gray arrows in Fig. 17a correspond to the height of the notch used to impose the displacement speed of the test ( $v = h\dot{\epsilon}$ ). This is an overall strain rate value since higher values will be encountered in the notched region. The overall load-displacement curves for the experiment and the 3D FE simulations are compared in Fig. 17b. It can be observed that the model does not predict accurately the experimental critical plastic strain. The simulated strain hardening is consistent with the experimental results. However, the model overestimates the value of the critical strain for all three tests. The constitutive model properly describes the

increasing amplitude of serrations depending on the geometry even though the stress drop level is under-estimated. Also, the frequency of serrations is higher in the simulations. It is shown below that these differences can be solved by the consideration of the machine stiffness. Fig. 17a shows the occurrence of instabilities inside the three notched geometries. Simulations demonstrate that smaller notch radii lead to a confinement of localization events in the notch region. The bands are then oriented perpendicular to the sollicitate axis. In contrast, inclined bands are observed in the NT10 specimen.

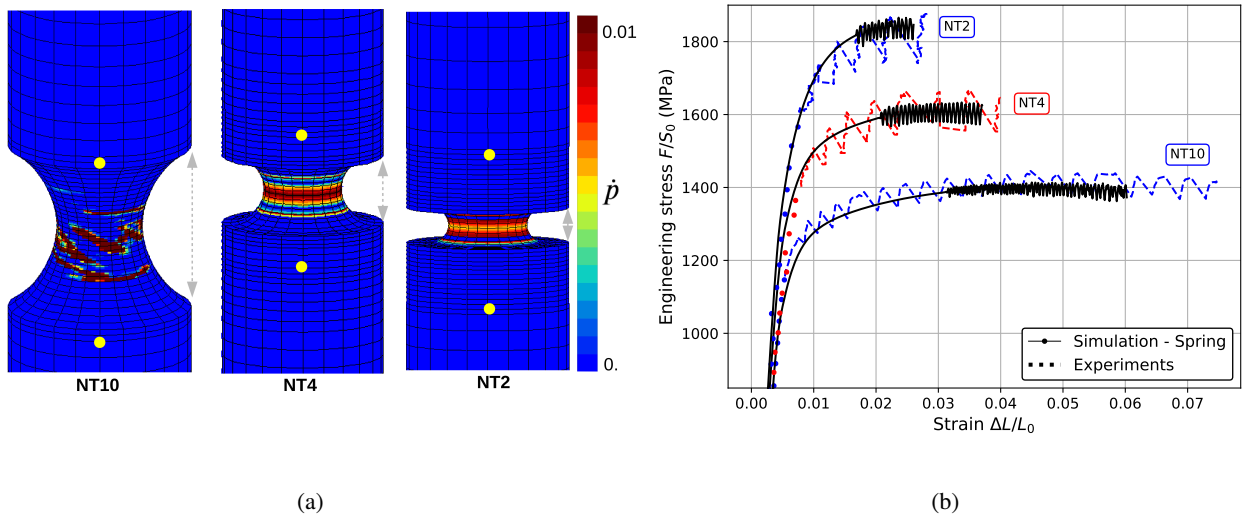


**Figure 17:** Displacement controlled tests on NT specimens at 500°C: a) Simulated plastic strain rate fields; b) Comparison between experimental and finite element simulation results for the stress vs. strain curves. The yellow points in Fig. 17a correspond to the 10 mm extensometric base ( $L_0$ ) chosen in agreement with the experimental and the gray arrows correspond to the height of the notches.

## 7. Discussion

This section discusses the previous experimental and simulation results to better assess the quality of the model. It also brings an essential aspect of the mechanics of PLC bands which was not considered in the previous simulations, namely the importance of the machine stiffness in the occurrence and type of serrations in the tensile curves. Finally the model is applied to structural computation of rotating turbine disks.

## 7.1. Validity range of the model

All the results presented above show that a rigorous identification strategy of the McCormick model allows to satisfactorily describe both macroscopic and local field measurements. A remarkable feature of the PLC effect is that the strain increments and corresponding stress drop amplitudes increase with increasing applied strain in all tests. This observation has already been made in the literature for other materials (Ranc and Wagner, 2005). The physical explanation put forward is that the average number of dislocations involved in the formation of a band increases with time due to a phenomenon of partial saturation of dislocations around the anchor points. The linear decomposition of the solute atom concentration  $C(p)$  and the plastic increment  $w(p)$ , both depending on the plastic strain in the model, allows to reproduce the increase of the stress drop amplitudes with increasing strain.

However a first limitation of the model was evidenced in section 6.4 in the case of tensile tests on notched (NT) specimens. The frequency and amplitude of serrations are not properly reproduced by the model, see Fig. 17b. It requires a more detailed analysis of the experimental results regarding these important features of the PLC effect. The description of the proposed improvement of the modeling approach with respect to these NT tests is postponed to section 7.2. The average frequency and magnitude of serrations observed on the macroscopic curves for each strain rate and for each of the three notched specimens are presented in table 4. The experimental results show that the period of occurrence of serrations increases, thus the frequency decreases, when the imposed strain rate decreases regardless of the geometry. As the motion of dislocations is slower at lower imposed strain rates, a larger proportion of dislocations are dragging solute atoms. When the concentration of solute atoms is high enough around dislocations, the dislocations are pinned thus inducing a longer waiting time. Moreover due to the larger proportion of dislocations pinned at low strain rates, when the external force is high enough to force the unpinning of dislocations and the rearrangement of solute atoms, the mean amplitude of stress drop on the curve is greater (Strudel, 1979). The inverse reasoning holds at higher imposed strain rates. The dislocations are mostly in the friction domain but a small proportion of them, due to a fast kinetics, end up being pinned by solute atoms. The mean stress drop is therefore smaller. The competition between the velocity of dislocations and the diffusion process of the solute atoms implies a transition of several types of PLC bands, generally called A, B or C in the literature, depending on the imposed strain rates. Even though the model can describe these three types and the transitions from one type to another during a simulation (see figure 10a), the frequency of the band formation is not well predicted for notched specimens (NT) in Fig. 17b. In addition the

table 4 indicates that both the frequency and the stress magnitude of serrations depend on the geometry. For instance, the NT2 specimen having the most severe notch, presents a longer period between serrations with a higher stress drop. As the plastic zone size is significantly reduced in this geometry, longer periods could be explained by the fact that the formation of each band is highly constrained and its propagation path more confined. Once all the conditions are satisfied for the band formation, the instability occurs and the corresponding stress drop is amplified by the triaxiality (stress concentration) caused by the notched geometry. The present statistical analysis of serrations is very limited since a detailed description would require a precise consideration of time stepping in the experiments and simulations which is out of the scope of the present study. Detailed analyses of experimental results were undertaken by Lebyodkin et al. (1996) in the case of tensile testing.

**Table 4**

Averaged period and magnitude of the serrations: Experimental values on NT specimens.

| Strain rate $s^{-1}$ | NT10       |           | NT4        |           | NT2        |           |
|----------------------|------------|-----------|------------|-----------|------------|-----------|
|                      | Period (s) | Mag (MPa) | Period (s) | Mag (MPa) | Period (s) | Mag (MPa) |
| $10^{-3}$            | 3.4        | 46.5      | 8.0        | 62.0      | 25.2       | 75.5      |
| $10^{-4}$            | 33.9       | 63.5      | 126.5      | 97.5      | 536.0      | 110.5     |
| $10^{-5}$            | 740.0      | 78.0      | 1670.5     | 110.      | -          | -         |

The second limitation of the model is the reproduction of the plastic strain rate carried by the band. Even though the model parameters have been calibrated on the 3D plate when the simulation is performed on the real geometry under displacement control, the strain rate inside the band can differ from the DIC measurements. However it is well known that for many mechanical localization phenomena, results depend on the mesh density. Benallal et al. (2006); Mazière et al. (2009) showed that the width of bands and the maximal plastic strain rate are mesh dependent, whereas their velocity or the amount of plastic strain carried are not. A solution could be to fix the element size of the simulation depending on DIC measurements although this would increase the already high calculation cost. Another approach to get rid of possible mesh dependence of the simulation results would be to introduce a characteristic length, typically associated with the width of the PLC band, into the constitutive model, as it is commonly done in strain gradient plasticity (Mazière et al., 2017; Hajidehi and Stupkiewicz, 2018). This approach has already been applied to

the simulation of the propagation of Lüders bands but it has not been considered yet for PLC banding.

## 7.2. Role of the machine stiffness

In the literature, only a few works take into account the machine stiffness in the modeling of DSA phenomena, although the importance of its effects has been reported in (Bodner, 1967; Cuddy and Leslie, 1972; Yamasaki et al., 2021). Belotteau et al. (2009) introduced a variable displacement rate loading, which is piecewise linear with time, into the simulation while the experiments are conducted at a constant crosshead displacement speed. Wang et al. (2011) introduced in 2D finite element calculations a layer of elements on top of the specimen with a representative stiffness equivalent to the machine stiffness. Even though the magnitude of the serrations predicted by the corresponding simulations were overestimated compared to those observed experimentally, he obtained a more accurate prediction of the experimental curves on a NT10 specimen especially regarding the morphology and frequency of PLC serrations. Each load drop corresponds to the appearance of a PLC band that creates an unloading of the spring representing the machine. The amplitude of the rising load for each serration corresponds to the loading phase of the spring. During the spring reloading, the zone of interest deforms very slightly, the elongation of the specimen remains almost constant until a new band appears in the sample.

According to Fig. 17b, the predicted amplitude of the oscillations as well as the critical plastic strain for the NT10 specimen are not in agreement with experimental observations. The finite element model of the sample has been modified to include an elastic spring on the bottom in series with the 3D specimen in order to account for the machine stiffness. The influence of several machine stiffness values ( $\text{N}\cdot\text{mm}^{-1}$ ) on the macroscopic curve is studied in Fig. 18a. The displacement is no longer applied on the bottom surface of the specimen, but on the bottom end of the spring. A constraint is applied to impose that the bottom surface remains flat and horizontal. Fig. 18a shows that the addition of a spring has a drastic effect on the amplitude of the serrations, their frequency, and the critical plastic strain. The softer the spring, the lower the frequency of the serrations, the lower the critical plastic strain, and the higher the amplitude of the serrations. The curves on Fig. 18a are plotted with an offset along the y-axis for better visualization. When the machine is very stiff, the load drops are vertical on the tensile curves whereas a soft machine leads to inclined load drops. The limit case is the force controlled test for which the inclined lines become horizontal as discussed in section 6.2.

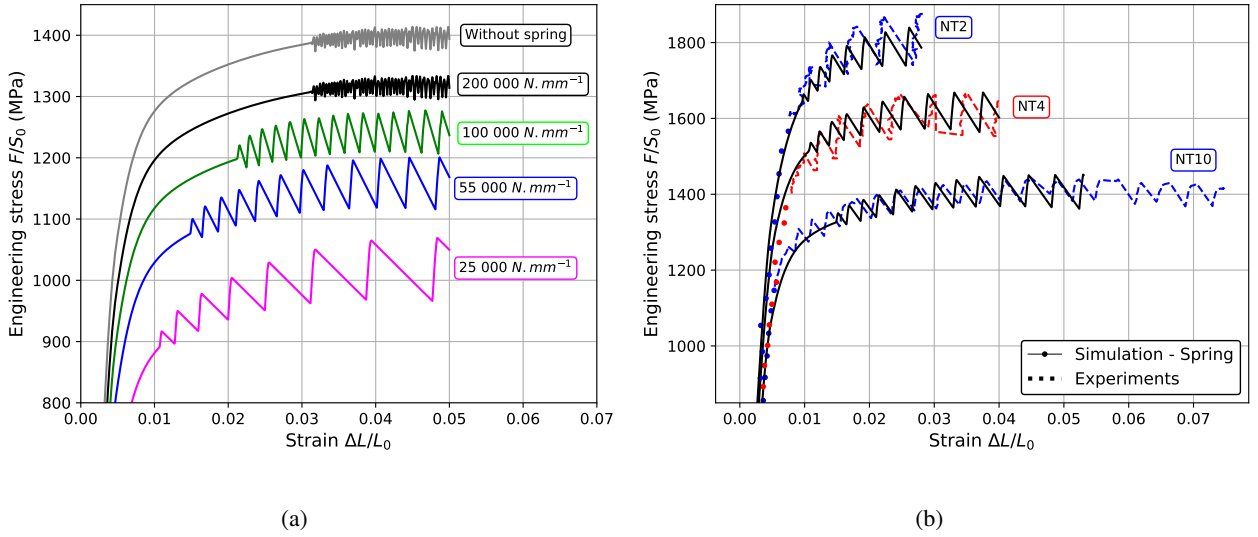


**Figure 18:** 3D simulations with added spring: a) Sensitivity study of the machine stiffness on macroscopic curve of NT10 specimen. Curves are plotted with an offset along the y-axis for better visualization; b) Real stiffness machine for the three notched specimens NT.

To make the machine stiffness value  $K_{machine}$  consistent with the experiment, the machine stiffness has been determined by comparison between two experimental curves: i) Force vs. machine cross-head displacement and ii) force vs. extensometer displacement. To determine the machine stiffness, the term  $F/K_{machine}$  is subtracted from the displacement of the machine curve such that  $K_{machine}$  allows the machine and extensometer curves to coincide. The machine stiffnesses calculated in that way are given in table 5 for the three NT specimen geometries. The 3D simulation results on these specimens using the actual machine stiffness are provided in Fig. 18b. The agreement between experiment and simulation is remarkable. Compared to the results of the model without a spring in Fig. 17b, the addition of a well-calibrated spring, representing the machine as an elastic body instead of a rigid body, allows to obtain much more accurate predictions. Moreover, due to less serrations on the macroscopic curve the cost of the simulation is reduced since higher time steps are allowed. It must be noted that the inclined slope of the load drop is properly described by the FE analysis which proves that the serration morphology is strongly dependent on the loading control of the machine. Note that it was not necessary to recalibrate the material parameters when accounting for the machine stiffness in the simulation of NT10 response. This is due to the fact that the machine stiffness did not affect significantly the tests on smooth specimens used for identification. However considering the machine stiffness right at



the beginning of the identification would improve the description of serrations and lead to improved set of parameters. It is concluded that the analysis of the PLC effect requires the consideration of the testing system as a whole including the specimen and machine response. In general, viscoelastic effects of the machine (gripping system etc.) are expected and result in different apparent stiffness depending on the strain rate. This aspect has not been investigated in the present work.

A zoom of the serrations in Fig. 18b is shown in Fig. 19. The curves are represented with points which correspond either to experimental acquisition either to numerical iterations. It can be noticed that no experimental points are captured during the inclined slope of the load drop due to the fact that the band is propagating too fast. On the contrary, in the simulation curve, numerous increments are necessary to reproduce the localization of a band. This imposes to have small time steps due to high heterogeneity of the plastic strain rate.

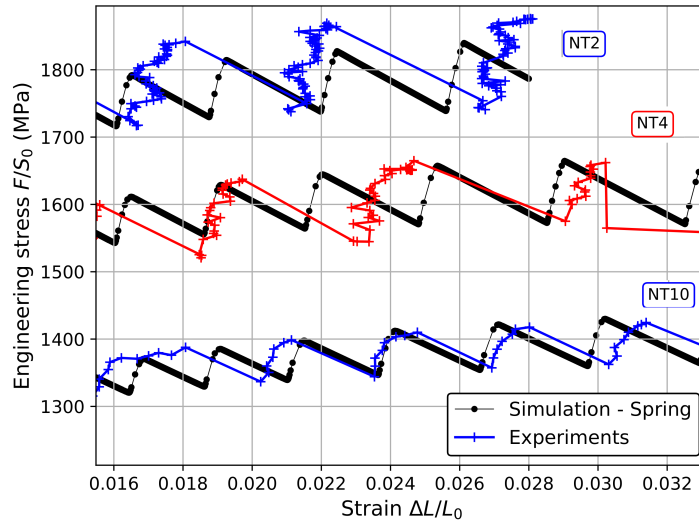


**Figure 19:** Zoom on the 3D simulations with added spring on the notched specimens NT. Points correspond either to extensometer acquisition either to calculation iterations.

**Table 5**

Machine stiffness values for three NT geometries. Mean value  $\pm$  standard deviation.

| Geometries                          | NT10               | NT4                | NT2                |
|-------------------------------------|--------------------|--------------------|--------------------|
| $K_{machine}$ (N.mm <sup>-1</sup> ) | 60,516 $\pm$ 1,450 | 61,388 $\pm$ 2,330 | 64,300 $\pm$ 1,804 |

In addition to the previous simulations, an hypothetic misalignment of the machine was investigated and modeled

by a transverse displacement along the perpendicular axis to the direction of loading via a second spring with an equivalent stiffness. The results showed that the critical plastic strain is not modified. The only impact is a slightly higher frequency of the appearance of the bands.

### 7.3. Turbine disk application

As the final goal is to predict instabilities in a rotating turbine disk, an application of the viscoplastic behavior, accurately calibrated on the previous specimens, is performed on a realistic structure. The simulation is carried out on a representative power turbine disk with slight geometry simplifications. An asymmetry between the top and the bottom sides (following y-axis) is introduced and five holes are added. The 3D simulation is performed on the entire disk due to the fact that instabilities can break the geometrical symmetry, as it was already observed in the previous specimens. A coarse mesh was used in the central area as opposed to a more refined mesh at the edges of the holes in the three space directions. This mesh allows to have a sufficient refinement while keeping a limited total number of degrees of freedom (40500 elements, 177414 nodes). The finite elements used are twenty-node quadratic elements with reduced integration (c3d20r and c3d15r). Sectional views of the mesh are shown in figure 20a and 20b. The computation is controlled by applying a centrifugal load. This load is updated and depends on the current configuration rather than the initial configuration for determining the new distances  $r$  of all points to the rotational axis as well as the direction of the centrifugal force. The Newton-Raphson algorithm rather than the arc-length method (where time is allowed to decrease) is used in this work because the viscosity in the material behavior of the material allows to overcome limit loads.

In many engineering finite element simulations of rotating disks, the inertial terms of the equilibrium equation are neglected, assuming that accelerations are usually low during most of the loading path. However, when the rotation rate reaches its limit value close to the burst of the disk, the accelerations can become significant. In order to estimate the impact of the inertial terms, two simulations are carried out: i) Quasi-static simulation with implicit resolution and ii) dynamic simulation with implicit resolution scheme. The global normalized rotation rate vs. normalized radial displacement at the rim of the disk is plotted in Fig. 21a.

For each simulation two normalized displacements curves at the rim of the disk are plotted: i) The displacement of the red point of Fig. 20a corresponding to a side without a hole in the left part of the mid-section, ii) the displacement

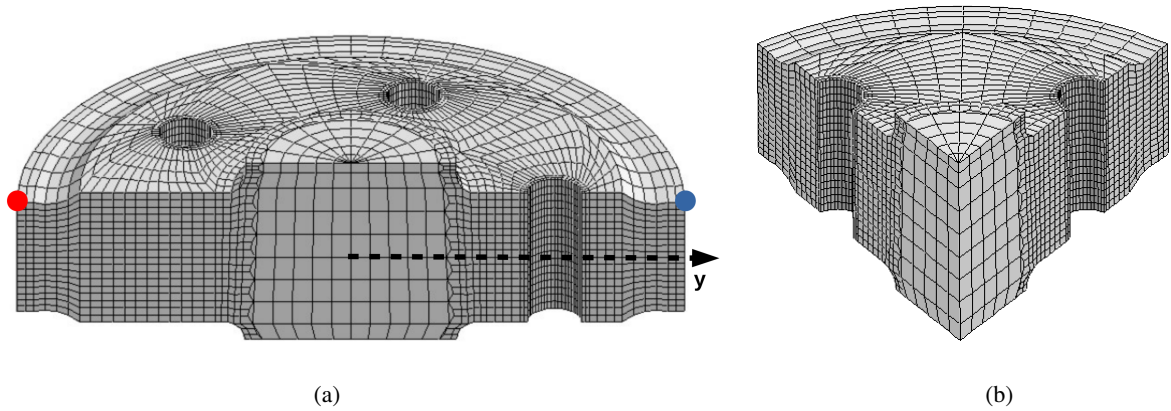


**Figure 20:** Sectional view of the 3D FE mesh of a representative turbine disk: a) Mid-section view of the mesh of the disk; b) One fifth section view of the mesh.

of the blue point of Fig. 20a corresponding to a side with a hole in the right part of the mid-section. It is observed in Fig. 21a that the simulated response of the disk is very similar to the one obtained in section 6.3 for a force-controlled tensile test. This confirms that the force-controlled tensile test is appropriate to evaluate the material response for turbine disk applications. Four steps can be distinguished on the curve with a significant increase (from 0.4% to 2.9%) of the displacement jumps. In addition the consideration of inertial effects in the simulation appears negligible regarding the global response of the disk. However a slight difference appears for the last step on the curve and the addition of the inertia terms delays the occurrence of instabilities. On the other hand, a mid-section of the disk without a hole is more massive than a mid-section containing a hole, so that its endpoint deforms more significantly. As a result, the disk deforms into a rounded star shape as shown in Fig. 21b on which the displacement evolution of the outer nodes of the specimen between the initial and deformed configurations is plotted. In addition it is noticed that the strain jumps (length of the steps on the curve) are higher for the side without a hole in figure 21a.

The occurrence of instabilities and the way they propagate at different times of the simulation are reported in Fig. 23 with the corresponding position (red or blue circles) on the global equilibrium curve in Fig. 22a. Due to the geometry, the plastic strain rate field of the disk (Fig. 22b) is heterogeneous. The plastic strain is concentrated around the holes along the radial axis. The maximal plastic strain is located perpendicularly to the tangent axis due to the fact that tangent stress is higher than radial ones. In addition, the plastic strain is positioned into a circular pattern around the central part of the disk. As a consequence the plastic strain rate is also heterogeneous and increases on the

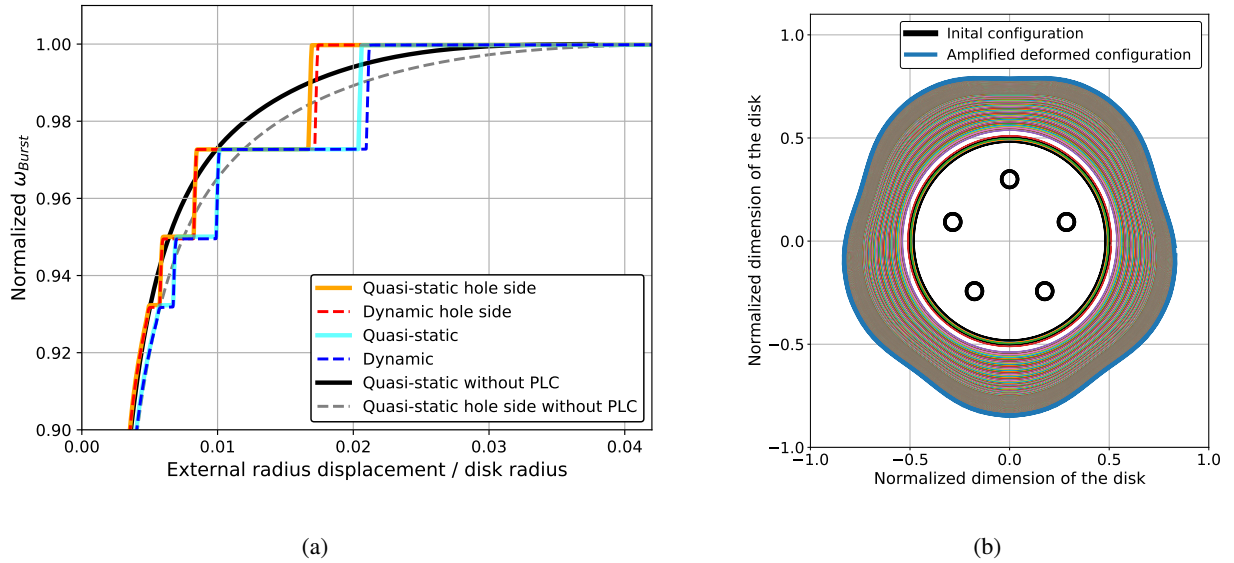


**Figure 21:** Simulated equilibrium curve of the turbine disk for i) static and ii) dynamic computations. The normalized imposed rotation rate vs. the displacement at the rim of the disk is plotted. For each simulation two displacements are shown: i) Node at the notched side (blue point in Fig. 20a), ii) node at the other side (red point in Fig. 20a).

same locations previously indicated. It drastically increases suddenly to form several propagative bands in a second step at the moment when a plateau is reached on the global curve. During the plateau the plastic strain rate continues increasing and redistributes to form a unique "band", that we call a strain burst band, on the whole disk. During this stage the disk is unstable and undergoes large strain jumps until the phenomenon repeats later or until the divergence of the simulation occurs. During these horizontal steps, the convergence of the implicit simulation is very hard (time increment very small around  $10^{-6}$  s) increasing considerably the number of increments (depending on the length of the plateau from 200 to more than 2000 increments). During rising phase (vertical phase) observed on the curve, the plastic strain rate remains constant reducing the number of necessary increments in the simulation (approximately 5 increments). In addition it can be noticed that the plastic strain rate field is symmetric during the first three stages and the symmetry is broken at the last stage in Fig. 23 at times 22 and 23 for instance. As the simulation is performed on the whole structure with the McCormick model, the computation cost and the memory storage (450 Go) of such a finite element model requires 40 days and high computing capacity (12 processors, Intel(R) Xeon(R) Gold 5118 CPU - 2.30GHz). A time independent elastoplastic simulation on the same disk geometry without PLC is also carried out (Fig. 21a). As expected, a faster result is obtained in that case with a computation time around 18 hours with the same

computation capacity than with PLC. The maximum load reached for all the calculations seem to be the same even though the divergence of the calculation without PLC occurs earlier.

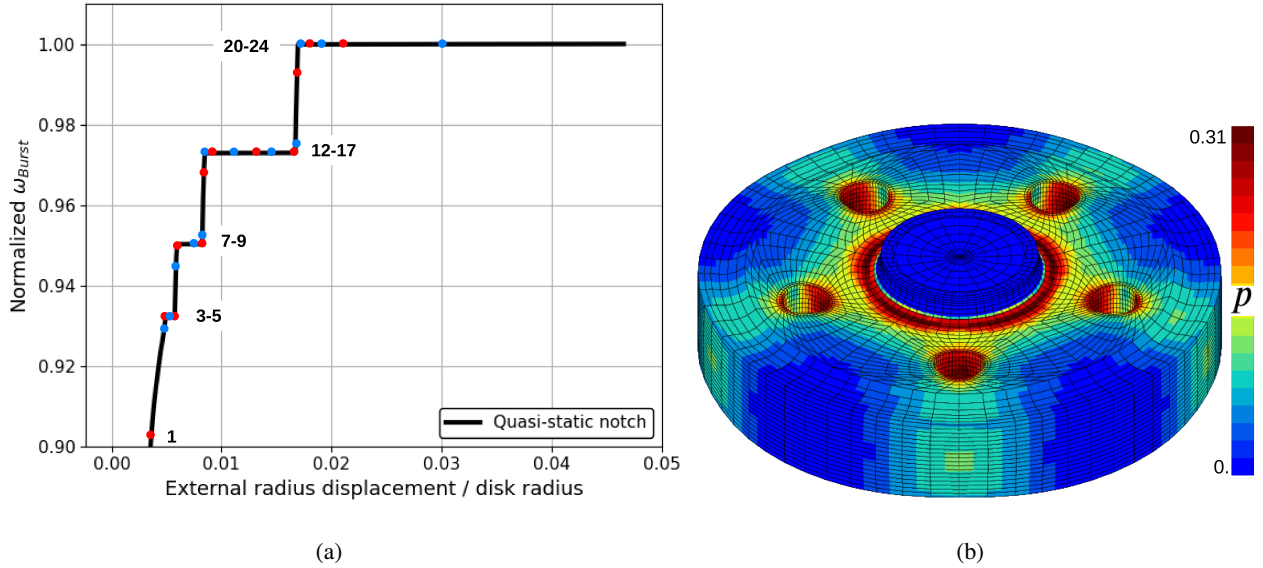


**Figure 22:** a) Simulated equilibrium curves of the turbine disk for static computation with associated numbers related to Fig. 23; b) Cumulative plastic strain field on the disk at the last increment.

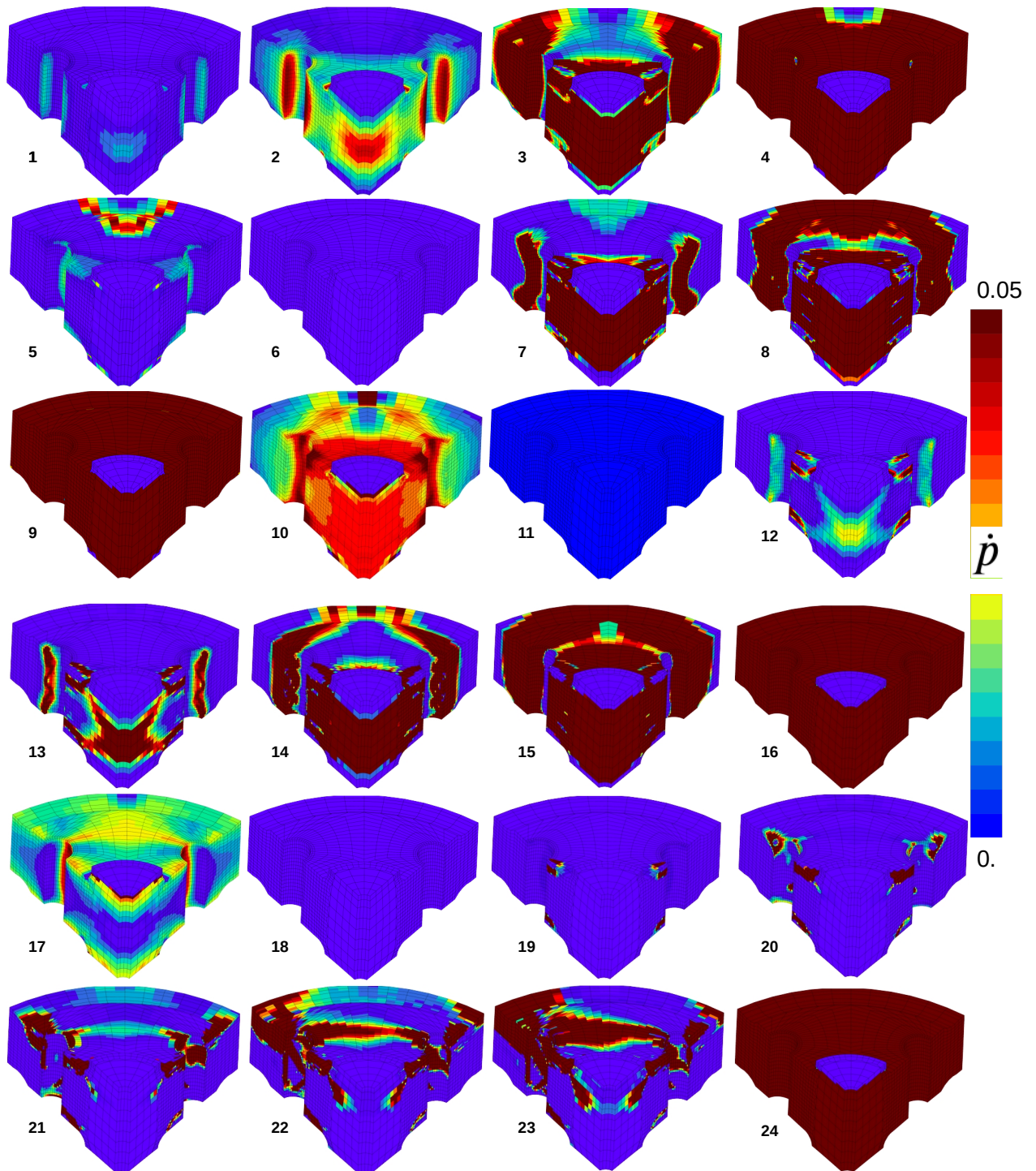


Figure 23: Simulated field of the plastic strain rate at several instants according to figure 22a on one fifth of the disk.

## 8. Conclusion

The main conclusions of the present work can be summarized as follows:

1. The Portevin-Le Chatelier effect is observed in the range of imposed strain rates between  $5 \cdot 10^{-6}$  and  $10^{-1} \text{ s}^{-1}$  at  $500^\circ\text{C}$  on Inconel718. All the specimen geometries, from smooth tensile to notched samples, display PLC instabilities: The higher the triaxiality, the higher the amplitude of the serrations and the lower their frequency. For comparison, at room temperature, the material exhibits only a slight positive strain rate sensitivity without serrations.
2. A original engraved speckle technique is proposed to perform accurate DIC measurements at high temperature. The DIC measurements reveal the dynamic process of the strain localization bands. The morphology of bands depends on the geometry: Inclined planar bands for flat specimens (D0), conical bands for smooth axi-symmetric specimens (ST), and, curved bands perpendicular to the loading axis for notched specimens (NT and DOE). The magnitude of the strain carried by the bands increases during the loading path until fracture. The period and the amplitude of serrations increase when the imposed strain rate decreases.
3. A McCormick-based viscoplastic constitutive model is identified from the response of all specimens with displacement-controlled loading. The identified model preserves both the negative strain rate sensitivity and the critical condition for the occurrence of serrations (critical strain).
4. It is demonstrated that the machine stiffness plays an essential role in the prediction of the amplitude and frequency of serrations and of the critical strain. The machine stiffness is introduced into the simulation by a linear spring with actual measured stiffness value. This fundamental aspect in the simulation of PLC phenomena has been overlooked in the previous literature.
5. The identified model accurately predicts the tensile response of specimens under force-control. Load drops observed in strain control tests are replaced by horizontal steps accompanied by strain bursts in fast propagating bands. The amounts of strain bursts and associated strain rates are accurately reproduced by the simulations.
6. A full 3D simulation on a representative high-pressure disk was performed using the identified constitutive model. It shows non-symmetric strain localization bands propagating through the disk. These simulations allow us to clearly identify the areas of initiation of these instabilities as the regions near the holes in the disk. Locally

the disk undergoes significant increases of radius which may play a role on the limit load at burst. Inertial terms in the mechanical formulation do not significantly affect the amplitudes of the serrations on the global curve. Note that all finite element simulations of the work are based on a large strain formulation of the model, an essential feature in the analysis of burst instabilities.

The use of PLC behavior in finite element simulations constitutes one of the main limitations to the industrial application due to the huge calculation cost and the various experimental testing needed to fully identify the behavior. This is why a model taking into account only the negative strain rate sensitivity without having instabilities during simulations has to be developed. The use of such a new model could be applied to the industrial application to better represent the hardening material at a lower imposed strain rate and the softening effect at a high imposed strain rate. A local fracture criterion can now be implemented based on all the tested specimens. A decoupled fracture function has to be fitted at both room and high temperatures. The influence of the PLC effect on fracture can now be analysed and the history of the triaxiality and the Lode parameter for instance can be compared with and without PLC effect, with and without consideration of the machine stiffness. This multiaxial fracture criterion model can be regarded as a new approach of the prediction of the maximal rotation speed of the disk at burst.

## References

- Amokhtar, H., Vacher, P., Boudrahem, S., 2006. Kinematics fields and spatial activity of Portevin-Le Chatelier bands using the digital image correlation method. *Acta Materialia* 54, 4365–4371. doi:<https://doi.org/10.1016/j.actamat.2006.05.028>.
- Aubert, Duval, 2021. URL: [https://www.aubertduval.com/wp-media/uploads/sites/2/pdf/PER718\\_FR.pdf](https://www.aubertduval.com/wp-media/uploads/sites/2/pdf/PER718_FR.pdf).
- Azadian, S., Wei, L., Warren, R., 2004. Delta phase precipitation in Inconel 718. *Materials Characterization* 53, 7–16. doi:<https://doi.org/10.1016/j.matchar.2004.07.004>.
- Belotteau, J., Berdin, C., Forest, S., Parrot, A., Prioul, C., 2009. Mechanical behavior and crack tip plasticity of a strain aging sensitive steel. *Materials Science and Engineering A* 526, 156–165.
- Benallal, A., Berstad, T., Borvik, T., Clausen, A., Hopperstad, S., 2006. Dynamic strain aging and related instabilities: experimental, theoretical and numerical aspects. *European Journal of Mechanics A/solids* 25, 397–424. doi:<https://doi.org/10.1016/j.euromechsol.2005.10.007>.
- Benallal, A., Berstad, T., Borvik, T., Hopperstad, O., Koutiri, I., Nogueira, R., 2008. An experimental and numerical investigation of the behaviour of AA5083 aluminium alloy in presence of the Portevin-Le Chatelier effect. *International Journal of Plasticity* 24, 1916–1945. URL: <https://doi.org/10.1016/j.ijplas.2008.03.008>.



- Besson, J., Cailletaud, G., Chaboche, J.L., Forest, S., Blétry, M., 2009. Non-Linear Mechanics of Materials. Solid Mechanics and Its Applications 167, Springer-Verlag Berlin Heidelberg. doi:10.1007/978-90-481-3356-7.
- Besson, J., Foerch, R., 1997. Large scale object-oriented finite element code design. Computer Methods in Applied Mechanics and Engineering 142, 165–187.
- Van den Beukel, A., 1980. On the mechanism of serrated yielding and dynamic strain ageing. Acta Metallurgica 28, 965–969.
- Bodner, S., 1967. The mechanics of repeated discontinuous yielding of metals. Materials Science and Engineering 2, 213–223. URL: [https://doi.org/10.1016/0025-5416\(67\)90061-4](https://doi.org/10.1016/0025-5416(67)90061-4).
- Böhlke, T., Bondar, G., Estrin, Y., Lebyodkin, M., 2009. Geometrically non-linear modeling of the Portevin-Le Chatelier effect. Computational Materials Science 44, 1076–1088. doi:<https://doi.org/10.1016/j.commatsci.2008.07.036>.
- Bridgman, P.W., 1952. Studies in large plastic flow and fracture with special emphasis on the effects of hydrostatic pressure. McGraw-Hill. doi:<https://doi.org/10.4159/harvard.9780674731349>.
- Cai, Y., Tian, C., Zhang, G., Han, G., Yang, S., Fu, S., Cui, C., Zhang, Q., 2017. Influence of  $\gamma'$  precipitates on the critical strain and localized deformation of serrated flow in Ni-based superalloys. Journal of Alloys and Compounds 690, 707–715. doi:<https://doi.org/10.1016/j.jallcom.2016.08.194>.
- Chaboche, J.L., Gaubert, A., Kanouté, P., Longuet, A., Azzouz, F., Mazière, M., 2013. Viscoplastic constitutive equations of combustion chamber materials including cyclic hardening and dynamic strain aging. International Journal of Plasticity 46, 1–22. doi:<https://doi.org/10.1016/j.ijplas.2012.09.011>.
- Chen, W., Chaturvedi, M., 1997. On the mechanism of serrated deformation in aged inconel 718. Materials Science and Engineering: A 229, 163–168. doi:[https://doi.org/10.1016/S0921-5093\(97\)00005-1](https://doi.org/10.1016/S0921-5093(97)00005-1).
- Clausen, A., Borvik, T., Hopperstad, O., Benallal, A., 2004. Flow and fracture characteristics of aluminium alloy AA5083-H116 as function of strain rate, temperature and triaxiality. Materials Science and Engineering 364, 260–272. doi:<https://doi.org/10.1016/j.msea.2003.08.027>.
- Cottrell, A., 1953b. Dislocations and Plastic Flow in Crystals. University Press, Oxford.
- Cuddy, L., Leslie, W., 1972. Some aspects of serrated yielding in substitutional solid solutions of iron. Acta Metallurgica 20, 1157–1167. doi:10.1016/0001-6160(72)90164-2.
- Cui, C., Gu, Y., Yuan, Y., Harada, H., 2011. Dynamic strain aging in a new Ni-Co base superalloy. Scripta Materialia 64, 502–505. URL: <https://doi.org/10.1016/j.scriptamat.2010.11.025>.
- Defaisse, C., Mazière, M., Marcin, L., Besson, J., 2018. Ductile fracture of an ultra-high strength steel under low to moderate stress triaxiality. Engineering Fracture Mechanics 194, 301–318. doi:<https://doi.org/10.1016/j.engfracmech.2017.12.035>.
- Devarapalli, R.S., Marin, E., Cormier, J., Le Gall, C., Franchet, J.M., Jouiad, M., 2016. Microstructure Evolution during Thermal Aging of Inconel 718. Springer International Publishing. pp. 11–18. doi:10.1007/978-3-319-48210-1\_2.
- Dhar, A., Clapham, L., Atherton, D., 2002. Influence of luders bands on magnetic Barkhausen noise and magnetic flux leakage signals. Journal of Materials Science 37, 2441–2446. doi:<https://doi.org/10.1023/A:1015419018741>.

- Dudova, N.R., Kaibyshev, R.O., Valitov, V.A., 2008. Manifestation of the Portevin-Le Chatelier effect in the Kh20N80 alloy. *The Physics of Metals and Metallography* 105, 98–104. doi:<https://doi.org/10.1134/S0031918X08010110>.
- Eiselstein, H.L., 1965. Metallurgy of a Columbium-Hardened Nickel-Chromium-Iron alloy. *Advances in the Technology of Stainless Steels and Related Alloys*, 62–79doi:<https://doi.org/10.1520/STP437335>.
- Fournier, L., Delafosse, D., Magnin, T., 2001. Oxidation induced intergranular cracking and Portevin-Le Chatelier effect in nickel base superalloy 718. *Materials Science and Engineering* 316, 166–173. doi:[https://doi.org/10.1016/S0921-5093\(01\)01224-2](https://doi.org/10.1016/S0921-5093(01)01224-2).
- Gao, M., Wei, R., 1995. Grain boundary  $\gamma''$  precipitation and niobium segregation in Inconel 718. *Scripta Metallurgica et Materialia* 32, 987–990. doi:[https://doi.org/10.1016/0956-716X\(95\)00062-Z](https://doi.org/10.1016/0956-716X(95)00062-Z).
- Garat, V., Cloue, J.M., Poquillon, D., Andrieu, E., 2008. Influence of Portevin-Le Chatelier effect on rupture mode of alloy 718 specimens. *Journal of Nuclear Materials* 375, 95–101. doi:<https://doi.org/10.1016/j.jnucmat.2007.10.009>.
- Graff, S., Forest, S., Strudel, J.L., Prioul, C., Pilvin, P., Béchade, J.L., 2004. Strain localization phenomena associated with static and dynamic strain ageing in notched specimens: experiments and finite element simulations. *Materials Science and Engineering A* 387–389, 181–185.
- Graff, S., Forest, S., Strudel, J.L., Prioul, C., Pilvin, P., Béchade, J.L., 2005. Finite element simulations of dynamic strain ageing effects at V-notches and crack tips. *Scripta Materialia* 52, 1181–1186.
- Guillermin, N., Köster, A., 2021. Laser engraving tracking technique for displacement field measurement. Patent FR2109996 .
- Hajidehi, M., Stupkiewicz, S., 2018. Gradient-enhanced model and its micromorphic regularization for simulation of Lüders-like bands in shape memory alloys. *International Journal of Solids and Structures* 135, 208–218. doi:<https://doi.org/10.1016/j.ijsoistr.2017.11.021>.
- Hale, C., Rollings, W., Weaver, M., 2001. Activation energy calculations for discontinuous yielding in Inconel 718SPF. *Materials Science and Engineering: A* 300, 153–164. doi:[https://doi.org/10.1016/S0921-5093\(00\)01470-2](https://doi.org/10.1016/S0921-5093(00)01470-2).
- Halim, H., Wilkinson, D., Niewczas, M., 2007. The Portevin-Le Chatelier (PLC) effect and shear band formation in an AA5754 alloy. *Acta Materialia* 55, 4151–4160. doi:<https://doi.org/10.1016/j.actamat.2007.03.007>.
- Hayes, R., 1983. On a proposed theory for the disappearance of serrated flow in f.c.c. Ni alloys. *Acta Metallurgica* 31, 365–371. doi:[https://doi.org/10.1016/0001-6160\(83\)90213-4](https://doi.org/10.1016/0001-6160(83)90213-4).
- Hosford, W., 2013. *Fundamentals of engineering plasticity*. Cambridge University Press.
- Jena, A.K., Chaturvedi, M.C., 1984. The role of alloying elements in the design of nickel-base superalloys. *Journal of Materials Science* 19, 3121–3139. doi:<https://doi.org/10.1007/BF00549796>.
- Kubin, L., Estrin, Y., 1991. Dynamic strain ageing and the mechanical response of alloys. *Journal de Physique III* 1, 929–943.
- Lebyodkin, M., Bréchet, Y., Estrin, Y., Kubin, L., 1996. Statistical behaviour and strain localization patterns in the Portevin–Le Chatelier effect. *Acta Materialia* 44, 4531–4541.
- Lee, S., Takushima, C., Hamada, J., Nakada, N., 2021. Macroscopic and microscopic characterizations of Portevin-Le Chatelier effect in austenitic stainless steel using high-temperature digital image correlation analysis. *Acta Materialia* 205, 734–754. URL: <https://doi.org/10.1016/j.actamat.2020.116560>.

- Levenberg, K., 1944. A method for the solution of certain problems in least squares. *Quarterly of Applied Mathematics* 2, 164–168.
- Louche, H., Bouabdallah, K., Vacher, P., Coudert, T., Balland, P., 2008. Kinematic Fields and Acoustic Emission Observations Associated with the Portevin Le Chatelier on an Al-Mg Alloy. *Experimental Mechanics* 48, 741–751. doi:<https://doi.org/10.1007/s11340-008-9125-5>.
- MacCormick, P., 1988. Theory of flow localisation due to dynamic strain ageing. *Acta Metallurgica* 36, 3061–3067.
- Marchenko, A., Mazière, M., Forest, S., Strudel, J.L., 2016. Crystal plasticity simulation of strain aging phenomena in  $\alpha$ -titanium at room temperature. *International Journal of Plasticity* 85, 1–33. doi:<https://doi.org/10.1016/j.ijplas.2016.05.007>.
- Máthis, K., Chmelík, F., Janecek, M., Hadzima, B., Trojanová, Z., Lukác, P., 2006. Investigating deformation processes in AM60 magnesium alloy using the acoustic emission technique. *Acta Materialia* 54, 5361–5366. doi:<https://doi.org/10.1016/j.actamat.2006.06.033>.
- Max, B., San Juan, J., Nò, M.L., Cloue, J.M., Viguier, B., Andrieu, E., 2018. Atomic species associated with the Portevin-Le Chatelier effect in superalloy 718 studied by mechanical spectroscopy. *Metallurgical and Materials Transactions A* 49, 2057–2068. doi:<https://doi.org/10.1007/s11661-018-4579-2>.
- Max, B., Viguier, B., Andrieu, E., Cloue, J., 2014. A re-examination of the Portevin-Le Chatelier effect in alloy 718 in connection with oxidation-assisted intergranular cracking. *Metallurgical and Materials Transactions A* 45, 5431–5441. doi:<https://doi.org/10.1007/s11661-014-2508-6>.
- Mazière, M., Andrebo, P.Q., 2015. Portevin-Le Chatelier effect under cyclic loading: experimental and numerical investigations. *Philosophical Magazine* 95, 3257–3277. doi:<https://doi.org/10.1080/14786435.2015.1049236>.
- Mazière, M., Besson, J., Forest, S., Tanguy, B., Chalons, H., Vogel, F., 2009. Overspeed burst of elastoviscoplastic rotating disks: Part II - Burst of a superalloy turbine disk. *European Journal of Mechanics* 28, 428–432. doi:<https://doi.org/10.1016/j.euromechsol.2008.10.002>.
- Mazière, M., Besson, J., Forest, S., Tanguy, B., Chalons, H., Vogel, F., 2010. Numerical aspects in the finite element simulation of the Portevin-Le Chatelier effect. *Computer Methods in Applied Mechanics and Engineering* 199, 734–754. doi:<https://doi.org/10.1016/j.cma.2009.11.004>.
- Mazière, M., Besson, J., Forest, S., Tanguy, B., Chalons, H., Vogel, F., 2010a. Numerical aspects in the finite element simulation of the Portevin-Le Chatelier effect. *Computer Methods in Applied Mechanics and Engineering* 199, 734–754.
- Mazière, M., Dierke, H., 2012. Investigations on the Portevin Le Chatelier critical strain in an aluminum alloy. *Computational Materials Science* 52, 68–72. doi:<https://doi.org/10.1016/j.commatsci.2011.05.039>.
- Mazière, M., Forest, S., Besson, J., Wang, H., Berdin, C., 2010b. Numerical simulation of the portevin le chatelier effect in various materials and at different scales. *Materials Science Forum* 638–642, 2670–2675.
- Mazière, M., Luis, C., Marais, A., Forest, S., Gaspérini, M., 2017. Experimental and numerical analysis of the Lüders phenomenon in simple shear. *International Journal of Solids and Structures* 106–107, 305–314.
- Miller, M., Babu, S., Burke, M., 2002. Comparison of the phase compositions in Alloy 718 measured by atom probe tomography and predicted by thermodynamic calculations. *Materials Science and Engineering* 327, 84–88. doi:[https://doi.org/10.1016/S0921-5093\(01\)01881-0](https://doi.org/10.1016/S0921-5093(01)01881-0).
- Nalawade, S., Sundararaman, M., Kishore, R., Shah, J., 2008. The influence of aging on the serrated yielding phenomena in a nickel-base superalloy.

- Scripta Materialia 59, 991–994. doi:<https://doi.org/10.1016/j.scriptamat.2008.07.004>.
- Ponnelle, S., Brethes, B., Pineau, A., 2002. High temperature fatigue crack growth rate in Inconel 718 : Dwell effect annihilations. European Structural Integrity Society 29, 257–266. doi:[https://doi.org/10.1016/S1566-1369\(02\)80082-6](https://doi.org/10.1016/S1566-1369(02)80082-6).
- Prasad, K., Sarkar, R., Ghosal, P., Kumar, V., 2010. Tensile deformation behaviour of forged disc of IN 718 superalloy at 650°C. Materials & Design 31, 4502–4507. doi:<https://doi.org/10.1016/j.matdes.2010.04.019>.
- Prasad, K., Varma, V.K., 2008. Serrated flow behavior in a near alpha titanium alloy IMI 834. Materials Science and Engineering 486, 158–166. doi:<https://doi.org/10.1016/j.msea.2007.09.020>.
- Ranc, N., Du, W., Ranc, I., Wagner, D., 2016. Experimental studies of Portevin-Le Chatelier plastic instabilities in carbon-manganese steels by infrared pyrometry. Materials Science and Engineering 663, 166–173. doi:<https://doi.org/10.1016/j.msea.2016.03.096>.
- Ranc, N., Wagner, D., 2005. Some aspects of Portevin-Le Chatelier plastic instabilities investigated by infrared pyrometry. Materials Science and Engineering 394, 87–95. doi:<https://doi.org/10.1016/j.msea.2004.11.042>.
- Ranc, N., Wagner, D., 2008. Experimental study by pyrometry of Portevin-Le Chatelier plastic instabilities-Type A to type B transition. Materials Science and Engineering: A 474, 188–196. doi:<https://doi.org/10.1016/j.msea.2007.04.012>.
- Ren, S., Mazière, M., Forest, S., Morgener, T.F., Rousselier, G., 2017. A constitutive model accounting for strain ageing effects on work-hardening. Application to a C–Mn steel. Comptes Rendus Mécanique 345, 908–921. doi:10.1016/j.crme.2017.09.005.
- Ren, S., Morgener, T., Mazière, M., Forest, S., Rousselier, G., 2020. Effect of Lüders and Portevin-Le Chatelier localization bands on plasticity and fracture of notched steel specimens studied by DIC and FE simulations. International Journal of Plasticity 136, 102880. doi:<https://doi.org/10.1016/j.ijplas.2020.102880>.
- Reyne, B., Manach, P.Y., Nicolas, M., 2019. Macroscopic consequences of Piobert-Luders and Portevin-Le Chatelier bands during tensile deformation in Al–Mg alloys. Materials Science and Engineering: A 746, 187–196. doi:<https://doi.org/10.1016/j.msea.2019.01.009>.
- Sims, C.T., Stoloff, N.S., Hagel, W.C., 1947. Superalloys II. Wiley.
- Song, R.H., Busso, E.P., Li, D.F., 2021a. Experimental and numerical investigations of dynamic strain ageing behaviour in solid solution treated Inconel 718 superalloy. Engineering Computations 38, 19–35. URL: <https://doi.org/10.1108/EC-01-2020-0006>.
- Song, R.H., Qin, H.L., Li, D.F., Bi, Z.N., Busso, E.P., Yu, H.Y., Liu, X.L., Du, J., Zhang, J., 2021b. An experimental and numerical study of quenching-induced residual stresses under the effect of dynamic strain aging in an IN718 superalloy disc. Journal of Engineering Materials and Technology 144. doi:10.1115/1.4051086.
- Strudel, J.L., 1979. Interactions des dislocations avec des impuretés mobiles, in: Groh, P., Kubin, L., Martin, J. (Eds.), Dislocations et déformation plastique, Yrvals, Les Editions de Physique. pp. 199–222.
- Swaminathan, B., Abuzaid, W., Sehitoglu, H., Lambros, J., 2015. Investigation using digital image correlation of Portevin-Le Chatelier Effect in Hastelloy X under thermo-mechanical loading. International Journal of Plasticity 64, 177–192. URL: <https://doi.org/10.1016/j.ijplas.2014.09.001>.
- Valerio, P., Gao, M., Wei, R., 1994. Environmental enhancement of creep crack growth in Inconel 718 by oxygen and water vapor. Scripta

## Portevin-Le Chatelier effect in a nickel-base superalloy for turbine disks

Metallurgica et Materialia 30, 1269–1274. doi:[https://doi.org/10.1016/0956-716X\(94\)90257-7](https://doi.org/10.1016/0956-716X(94)90257-7).

Vic-2D, . URL: <https://www.correlatedsolutions.com/vic-2d/>.

Wang, H., Berdin, C., Mazière, M., Forest, S., Prioul, C., Parrot, A., Le-Delliou, P., 2011. Portevin-Le Chatelier (PLC) instabilities and slant fracture in C-Mn steel round tensile specimens. Scripta Materialia 64, 430–433. doi:<https://doi.org/10.1016/j.scriptamat.2010.11.005>.

Wang, H., Berdin, C., Mazière, M., Forest, S., Prioul, C., Parrot, A., Le-Delliou, P., 2012. Experimental and numerical study of dynamic strain ageing and its relation to ductile fracture of a C-Mn steel. Materials Science and Engineering 547, 19–31. doi:<https://doi.org/10.1016/j.msea.2012.03.069>.

Yamasaki, S., Miike, T., Mitsuhashi, M., Nakashima, H., Akiyoshi, R., Nakamura, T., Kimura, S., 2021. Quantitative analysis of the Portevin-Le Chatelier effect by combining digital image correlation and dead-weight-type tensile test. Materials Science and Engineering 816, 213–223. doi:<https://doi.org/10.1016/j.msea.2021.141277>.

Yilmaz, A., 2011. The Portevin-Le Chatelier effect: a review of experimental findings. Science and Technology of Advanced Materials 12, 063001. doi:<https://doi.org/10.1088/1468-6996/12/6/063001>.

Zhang, H., Zhang, S., Cheng, M., Li, Z., 2010. Deformation characteristics of  $\delta$  phase in the delta-processed Inconel 718 alloy. Materials Characterization 61, 49–53. doi:<https://doi.org/10.1016/j.matchar.2009.10.003>.

Zhang, S., MacCormick, P., Estrin, Y., 2001. The morphology of Portevin-Le Chatelier bands : finite element simulation for Al-Mg-S. Acta Materialia 49, 1087–1094.

Zhang, X., Dong, R., Zhao, Y., Liu, D., Yang, L., Hou, H., 2021. Serrated flow behaviors in a Ni-based superalloy. Material Research Express 8, 026515. doi:<https://doi.org/10.1088/2053-1591/abe0f2>.